Rheol Acta (2008) 47:841–859
DOI 10.1007/s00397-007-0253-0

ORIGINAL CONTRIBUTION

# Effect of a controlled pre-deformation history on extensional viscosity of dilute polymer solutions

**Shelley L. Anna · Gareth H. McKinley**

Received: 10 November 2007 / Accepted: 25 November 2007 / Published online: 7 March 2008


**Abstract** We use a modified filament stretching rheometer to quantify the influence of a known controlled pre-shear history on the transient extensional viscosity of a dilute polymer solution. Two different types of pre-deformation are explored; both influence the subsequent stretching significantly, albeit in opposite ways. Small-amplitude oscillatory straining parallel to the direction of stretching enhances strain hardening and accelerates the tensile stress growth toward the steady-state value. Conversely, steady torsional shearing orthogonal to the direction of stretching retards strain hardening and results in a delayed approach to steady-state elongational flow. In both cases, the final steady-state extensional viscosity is the same as that observed with no pre-shearing. Calculations using a finitely extensible nonlinear elastic Peterlin dumbbell model qualitatively capture the trends observed in experiments, enabling interpretation of these observations in terms of the degree of polymer chain stretching imposed by the flow before extensional stretching.

**Keywords** Uniaxial extension · Shear history · Polymer solution · Filament stretching

S. L. Anna (✉)
Department of Mechanical Engineering,
Carnegie Mellon University,
5000 Forbes Avenue,
Pittsburgh, PA 15213-3980, USA
e-mail: sanna@cmu.edu

G. H. McKinley
Department of Mechanical Engineering,
Massachusetts Institute of Technology,
77 Massachusetts Avenue,
Cambridge, MA 02139, USA

## Introduction

Accurate measurement of the extensional viscosity of polymeric liquids has been a significant challenge in rheology over the past two decades, particularly for mobile liquids such as polymer solutions (Petrie 2006). Numerous techniques have been developed to address this need and they may be broadly categorized into entry flows (Binding 1993), stagnation point flows (Hermansky and Boger 1995; Lee and Muller 1999), and stretching flows (Jones et al. 1987). A "round robin" study (Sridhar 1990) comparing measurements from many different devices showed over three decades of variation in the apparent elongational viscosity $\eta_E$. In a review of these techniques, James and Walters (1994) note that the "values of $\eta_E$…are transient… and the disparity makes it clear how strongly these values depend upon variables other than strain rate." The discrepancies between the measurements arise from at least three major factors: a pre-shear history that is poorly characterized and difficult to eliminate, shear flow components originating from nearby walls, and an inability to monitor the transient evolution of stresses.

The filament stretching rheometer (Sridhar et al. 1991; Tirtaatmadja and Sridhar 1993) addresses all of these issues. In this device, a small volume of fluid is placed between two circular endplates which are separated with a prescribed velocity such that a nearly ideal uniaxial extensional flow is imposed. Independent measurement of the force on the endplate and the mid-filament diameter enables the *evolution* of stresses in the fluid element near the midplane to be monitored from equilibrium (i.e., no pre-shear history) to steady-state extension. Contributions from shearing deformations are confined to a small region near the endplates. Over the past decade, the filament stretching technique has matured into a quantitative rheological tool

(Anna et al. 2001; McKinley and Sridhar 2002). Recent studies have focused on dilute polystyrene solutions (Gupta et al. 2000), dilute λ-DNA solutions (Sunthar et al. 2005), monodisperse and bidisperse solutions (Ye et al. 2003), semidilute and entangled solutions (Bhattercharjee et al. 2002; Rothstein and McKinley 2002a; Bhattacharjee et al. 2003), high temperature melts (Bach et al. 2003a; Bach et al. 2003b; Rasmussen et al. 2005; Nielsen et al. 2006), branched polymer solutions (Ye and Sridhar 2001), associative polymers (Tripathi et al. 2006), and wormlike micellar solutions (Rothstein 2003). In addition, filament stretching has been combined with optical birefringence measurements to obtain simultaneous stress growth and chain conformation measurements (Doyle et al. 1998; Rothstein and McKinley 2002a, b).

The ability to observe single-molecule dynamics both experimentally and through Brownian dynamics simulations has developed concurrently with the filament stretching rheometer. Numerous studies have revealed mechanisms by which individual molecules interact and unravel in flows, resulting in macroscopic stress growth. Filament stretching measurements provide an important connection between molecular-level experiment/simulation and macroscopic flow response. Larson (2005) describes several areas in which these distinct approaches have together led to a deeper understanding of the behavior of flexible polymers in flow. For example, combined experiment and simulation has led to a better understanding of hydrodynamic interaction and solvent quality. Hydrodynamic interaction has been modeled via conformation-dependent drag (Magda et al. 1988), leading to conformation hysteresis due to the large disparity between drag on the chains in the coiled and stretched states. The effect is more pronounced for polystyrene than for λ-DNA, and it is more important in extensional flow than in shear flow (Schroeder et al. 2004; Schroeder et al. 2005; Sunthar et al. 2005). Hydrodynamic interaction slows the unraveling of the chain (Agarwal 2000; Hsieh and Larson 2004), delaying the onset of strain hardening compared to the case with no hydrodynamic interaction (Hsieh et al. 2003; Hsieh and Larson 2004). The steady-state plateau in the stress growth does not depend upon the inclusion of hydrodynamic interaction. Excluded volume repulsions simulate the influence of solvent quality on the polymer stretch profile (Solomon and Muller 1996b; Li and Larson 2000; Sridhar et al. 2000), leading to the start of stress growth approximately one Hencky strain unit earlier in the case of a good solvent compared with a theta solvent for the same polymer molecular weight. This accelerated stress growth can be understood in terms of the initial polymer chain configuration; in the case of a good solvent, the initial coil size is larger, and thus, the molecule can become highly stretched more quickly. Clearly, the transient response of a polymer solution to an extensional flow is a sensitive indicator for any factor that influences the chain conformation from the start of stretching through the transient growth to steady state extension (Li and Larson 2000).

Brownian dynamics simulations and single-molecule observations of stretching DNA reveal a significant amount of heterogeneity in the chain stretch profile among individual polymer chains experiencing extensional flow (Doyle et al. 1998; Smith and Chu 1998; Larson et al. 1999; Larson 2005). Heterogeneity occurs as a result of different initial conformations as the polymer chains enter the extensional flow region. Molecular stretching is impeded by an initially folded conformation (Larson et al. 1999; Larson 2005). Larson (2000) and Agarwal (2000) independently used Brownian dynamics simulations to examine the influence of "pre-conditioning" of the polymer chains before their entry into the extensional flow region. Larson observed that pre-shearing before extension reduces the occurrence of folds and kinks in the stretched chain conformation. The effect is most pronounced when the pre-conditioning involves a simple shear flow parallel to the direction of stretching, in which case, the transient tensile stresses approach steady state *more rapidly* than in the case without pre-shearing.

Other studies reveal that pre-shearing influences coil–stretch hysteresis. Pre-shearing leads to partial stretching, allowing the molecules to be more easily stretched in a subsequent extensional flow as a result of conformation-dependent drag (Schroeder et al. 2003; Hsieh and Larson 2005). As faster pre-shearing leads to a larger initial stretch, the critical strain rate for the coil–stretch transition is expected to decrease as the pre-shear rate increases (James et al. 1987; Larson and Magda 1989; Larson 2000). In addition, the influence of pre-shearing on the coil–stretch transition is more pronounced at higher molecular weights and with stronger hydrodynamic interactions. Accessing the relevant flow regime to observe the coil–stretch transition experimentally remains a significant challenge; however, recent filament stretching experiments probing the behavior of dilute polystyrene solutions near the coil–stretch transition reveal many of the behaviors expected from Brownian dynamics simulations, including a significant non-ergodic or "glassy" dependence of the measured response on strain history (Sridhar et al. 2007).

Brownian dynamics simulations can reveal details of the molecular behavior underlying the response of dilute polymer solutions to complex flows. However, the influence of pre-conditioning and mixed shear and extensional flows has been largely untested in experiment. In part, this is due to significant practical difficulties in accessing and controlling these flows in a way that can be consistently compared with simulations. While the filament stretching device has been successful in *isolating* extensional flow from shearing components present in other elongation-

dominated flows, other methods such as entry flows better mimic the complex mixed-kinematic flows used in many industrial processes. However, the role of shearing and pre-deformation history cannot be systematically decoupled from that of elongation in most of these methods. The ability to decouple these two effects and to systematically vary the deformation history before imposing elongational flow is important both to enhance our fundamental understanding of the polymer dynamics in complex flows as well as to enable optimization of relevant processes involving complex flows (Larson 2005). These include, among others: polymer processing flows, flow through porous media for applications such as enhanced oil recovery (Jones and Walters 1989; Vorwerk and Brunn 1991; Evans et al. 1994), benchmark flows such as flow past a sphere and contraction flows (Satrape and Crochet 1994; Solomon and Muller 1996a), and turbulent drag reduction (Graham 2004). For turbulent drag reduction in particular, recent experimental and numerical studies have elucidated the mechanisms for enhanced drag reduction by polymer additives (Toms 1977; Graham 2004). Among other things, the large extensional viscosity of polymer solutions is a primary factor, and pre-shearing in the near-wall region has been shown to enhance stretching (Donohue et al. 1972; Tiederman et al. 1985; Vissmann and Bewersdorff 1990; Massah et al. 1993; Ilg et al. 2002; Zhou and Akhavan 2003) by modifying the transient chain conformation as it enters local stretching regions just outside the near-wall region (Massah et al. 1993; Dubief et al. 2004). Clearly, fully developed turbulence consists of a very complex mixture of shear and elongation, and decoupling these competing effects on the polymer chain dynamics is difficult in mixed flows. We seek a flow in which we can independently control the two effects.

The few experimental studies attempting to isolate and control the pre-shear history include two studies which use Poiseuille flow in a channel (James et al. 1987) and a concentric cylinder device (Vissmann and Bewersdorff 1990), respectively, to impose shearing immediately before extrusion of a polymer solution through a converging orifice. Although the extrusion flow imposes an inhomogeneous elongation rate, both studies show that increasing the average pre-shear rate leads to an increase in the apparent elongational viscosity of polyethylene oxide solutions at a fixed elongation rate. Separately, a pressure-sensitive adhesive was exposed to varying pre-strain history in an Instron device (Ferguson et al. 1998). The sample was stretched using two sequential constant velocities, and the transient tensile stress growth varied depending on whether the first velocity was larger or smaller. In all experiments, the stress growth converged after an initial transient period. The influence of initial conditions in a spinline rheometer has been investigated through careful analysis of the kinematics along the filament, measurement of the axial force at the die exit, and accurate control of the steady flow rate and the applied tension, allowing for the specification of initial conditions on the radial and axial stresses (Ramanan et al. 1997; Bechtel et al. 2001). In direct numerical simulations of finitely extensible nonlinear elastic (FENE) chains in simple rheological flows, Massah et al. (1993) observed that pre-shearing perpendicular to the stretching direction delays unraveling of the FENE chains. However, this delay did not increase monotonically with pre-shear rate; in fact, large rotation rates were found to result in minor delays in the onset of chain stretching, while small rotation rates led to significant delays.

The most recent and most careful studies of mixed flows to date involve both experimental observations of DNA conformation and Brownian dynamics simulations (Babcock et al. 2003; Schroeder et al. 2003, 2004, 2005; Woo and Shaqfeh 2003). In these studies, a flow type parameter is used to combine different levels of shear and extension simultaneously in a given flow. The flow type parameter was originally used to describe mixed shear and elongational flows generated in a four roll mill (Fuller and Leal 1980). In the early studies, the flow-induced birefringence was measured for polystyrene solutions in mixed flows, as a function of flow type, flow strength, and polymer molecular weight. A key observation from this work is that the birefringence measurements collapse onto a single curve when plotted as a function of the extensional component of the velocity gradient (Fuller and Leal 1980). The recent studies build on this idea by observing the evolution of individual chain conformations in mixed flows, comparing Brownian dynamics simulations (incorporating both excluded volume and hydrodynamic interaction) with fluorescence imaging of individual DNA molecules in flow. In these studies, the polymer chains exhibit a significant conformation hysteresis, switching between either a coiled or a highly stretched state depending on the deformation history (Schroeder et al. 2003). Simulations of the transient polymer conformation agree well with experiments over a wide range of DNA strand lengths in both shearing and extensional flows (Schroeder et al. 2004, 2005). As in the early studies of Fuller and Leal, the average stretch of a polymer chain at steady state is found to depend only on the extensional component of the flow and is independent of the magnitude of shearing. In nearly pure shearing flows, large fluctuations in the extension of the polymer chain are observed (Babcock et al. 2003), and the nature of the transition between coiled, tumbling, and stretched states depends on the flow type (Woo and Shaqfeh 2003). Even in flows that are nearly purely shearing, the stretching of the polymer chain depends only on the extensional component of the flow, although stretching occurs significantly more slowly than in

purely extensional flows (Hur et al. 2002). Brownian dynamics simulations of combined shear and extensional flows using the FENE-ALS adaptive length scale model (Ghosh et al. 2001; Ghosh et al. 2002) show that when chains that are initially oriented parallel or perpendicular to the stretching direction enter a region of elongational flow, the onset of chain stretching is accelerated or delayed respectively.

Brownian dynamics simulations and single-molecule visualization are effective tools for examining polymer chain dynamics in viscous flows. However, this combined approach can only provide information about the transient polymer conformation, and not the evolution of the tensile stresses in the polymer solution. The filament stretching rheometer offers a unique opportunity to connect the molecular conformation and the macroscale stress evolution (Sridhar et al. 2007). It also offers direct control over the amount and type of shearing flow imposed *just before* nearly ideal uniaxial stretching. In the present paper, we systematically impose a known and controlled pre-shearing history on a fluid filament immediately before a nearly ideal uniaxial elongational flow in the filament stretching device. Our rheometer has been modified to apply either steady, torsional shear flow orthogonal to the stretching direction, or oscillatory squeeze flow parallel to the stretching direction. In the following sections, we show that the fluid response to these initial shearing flows agrees with the material functions measured using conventional shear rheometry techniques. We then examine the effect of the two types of pre-deformation histories on the fluid response to the subsequent stretching flow. Finally, we use the FENE-Peterlin (FENE-P) constitutive equation (Bird et al. 1987b) to model the transient response of a material element to a homogeneous uniaxial elongational flow which is imposed subsequent to the pre-shear flow, and we compare the results from experiments and simulations. We note that a similar experimental approach has been utilized in a recent study focusing on wormlike micellar solutions (Bhardwaj et al. 2006). In this case, the pre-shearing flow is a torsional shear flow orthogonal to the direction of stretching, and the pre-shear rates are varied such that shear banding occurs at the highest rates. The duration and rate of pre-shearing influences the stress at rupture of the filament and delays the onset of strain hardening. Pre-shearing in the shear-banding regime leads to a dramatic reduction in strain hardening in subsequent stretching, presumably due to significant breakdown of the micellar network.

## Materials and methods

Our test fluid for the present study is a dilute solution ($c$= 0.025 wt%) of high molecular weight polystyrene dissolved in oligomeric styrene oil (Hercules Piccolastic A5 Resin). This fluid, denoted PS025, is a model elastic liquid, or "Boger fluid", designed to have nearly constant shear viscosity and high elasticity (Boger 1977/1978). The high molecular weight polystyrene (Scientific Polymer Products) has a weight-averaged molecular weight of $M_w$=2.25×$10^6$ g/mol and a narrow polydispersity (PDI≅1.02), as reported by the manufacturer and measured independently via gel permeation chromatography. The density of the fluid is $\rho$=1.026 g/cm$^3$ at $T$=25 °C. The surface tension is $\sigma$= 0.0378 N/m as measured using a Wilhelmy plate in a Krüss digital tensiometer (Model K10ST). The PS025 solution can be considered dilute based on an estimate of the overlap concentration,

$$c^* = \frac{M_w}{4/3\pi R_g^3 N_A} = 0.076 \text{ wt\%}, \quad (1)$$

which is significantly larger than our solution concentration ($c/c^*$=0.33). In the above equation, $N_A$ is Avogadro's number and $R_g$ is the radius of gyration given by $R_g^2 = C_\infty n l^2$. For polystyrene, $C_\infty = 9.85$ (Brandrup et al. 1999), $n = 2M_w/M_0$ is the number of carbon–carbon bonds in the backbone, and $l$=1.54 Å is the length of a carbon–carbon bond (Flory 1953).

The steady and dynamic shear rheology of the PS025 solution was characterized using a TA Instruments AR1000N cone-and-plate rheometer, and steady shear flow measurements were also performed using a Rheometrics RMS-800 cone-and-plate rheometer to obtain values of the first normal stress coefficient, $\Psi_1(\dot{\gamma})$. Measurements were taken at three temperatures, 15, 25, and 35 °C, and time–temperature superposition was used to obtain master curves for the steady and dynamic material functions over six decades in shear rate. The resulting material functions are plotted in Fig. 1. From these measurements, we extract values of the zero-shear-rate viscosity, $\eta_0$=24.9 Pa s, and the solvent viscosity in the high frequency limit, $\eta_s$= 21.9 Pa s. In addition, we fit the linear viscoelastic data using a Zimm bead-spring model to obtain a spectrum of relaxation times (Bird et al. 1987b) and obtain a longest relaxation time of $\lambda_z$=3.9 s. The resulting fitted curves are also shown in Fig. 1. A small amount of solvent elasticity is needed to describe the high frequency behavior observed in the storage and loss moduli. In this case, the solvent relaxation time and modulus are, respectively, $\lambda_s$=2.7×$10^{-4}$ s, $G_s$=8.1×$10^4$ Pa.

## Two types of pre-deformation history

In the present paper, we explore two methods of experimentally controlling the initial conformations of the

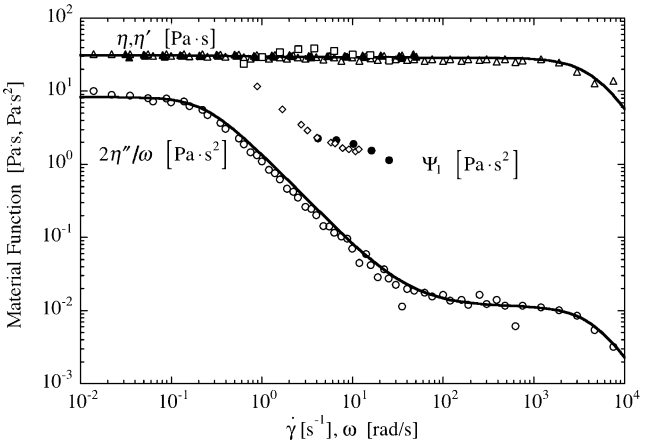


**Fig. 1** Steady and dynamic shear material functions for the PS025 fluid obtained from oscillatory squeeze flow (*open square*, $\eta'(\omega)$) and steady torsional flow (*open diamond*, $\Psi_1(\dot{\gamma}_R)$) measurements in the filament stretching device. Measured material functions agree well with those obtained using a conventional cone-and-plate rheometer (*filled triangle*, $\eta(\dot{\gamma})$; *filled circle*, $\Psi_1(\dot{\gamma}_R)$; *open triangle*, $\eta'(\omega)$, *open circle*, $2\eta''(\omega)/\omega$). *Solid curves* represent fits to a Zimm spectrum of relaxation times

polymer chains in solution just before stretching. These two techniques are illustrated in Fig. 2. To orient the polymer chains along the stretching direction, we impose an oscillatory squeeze flow between the two rigid endplates in a filament stretching device (Fig. 2b). We examine the role of oscillation amplitude, $l_0$, and frequency, $\omega$, on the molecular orientation, and thus, on the subsequent transient extensional stress growth. To orient the polymer chains orthogonal to the stretching direction, we impose a steady shear flow by rotating the upper endplate at a steady rate $\Omega$ (Fig. 2a). The degree to which the molecules are oriented normal to the stretching direction is dependent on the rotation rate, and thus the transient stress growth during extension is also expected to depend on this initial rotation rate. The filament stretching device used in this study has been described in detail previously (Anna et al. 2001). This device has been modified to impose either of the two types of pre-deformation history described here, as depicted schematically in Fig. 2.

## Oscillatory pre-straining parallel to direction of stretching

To realize oscillatory squeeze flow parallel to the stretching direction, a cyclic motion profile is downloaded to the linear motors that control the endplates. During the squeeze flow, the upper endplate moves according to

$$L_p(t) = L_0 + l_0 \sin \omega t \tag{2}$$

where $l_0$ is the amplitude of oscillation and $\omega$ is the angular frequency. Differentiating Eq. 2, the corresponding velocity of the upper endplate is given by

$$\dot{L}_p(t) = \omega l_0 \cos(\omega t). \tag{3}$$

The range of available frequencies is approximately $0.6 \leq \omega \leq 125$ rad/s, and the minimum amplitude of oscillation is about 0.01 cm (100 μm). In addition, the amplitude

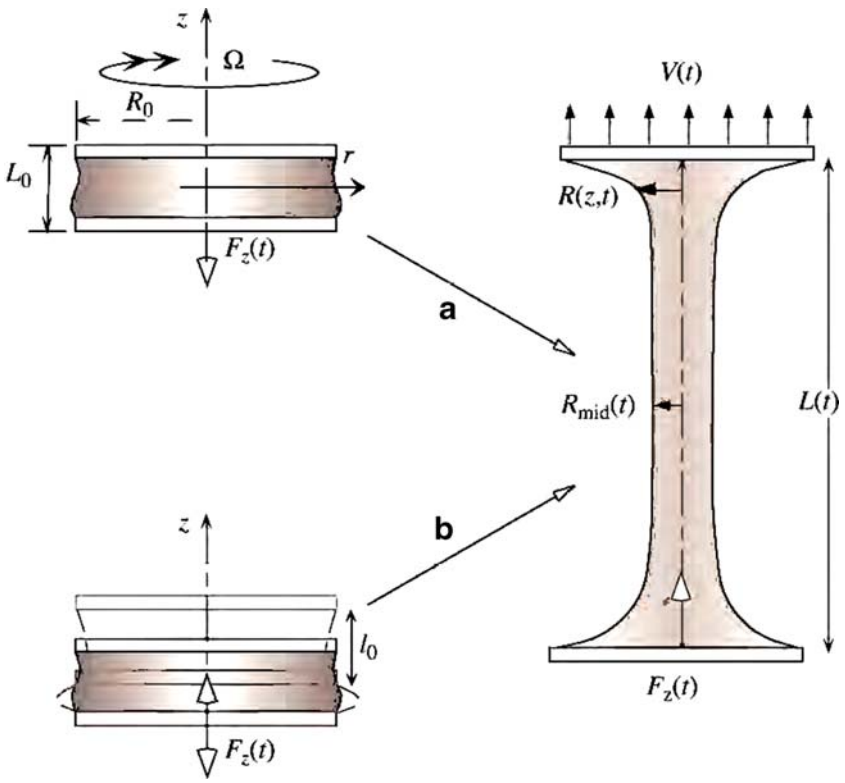


**Fig. 2** Schematic diagram of two types of controlled pre-deformation history imposed before a nearly uniaxial extensional flow in a filament stretching device. **a** Steady torsional flow with principal flow direction normal to stretching direction, in which $\Omega$ is the rotation rate of the upper endplate; **b** Oscillatory squeeze flow with principal flow direction parallel to stretching direction in which $f$ is the frequency of oscillation of the upper endplate and $l_0$ is the amplitude of oscillation

of oscillation cannot exceed the gap between the plates, $L_0$. Typical amplitudes of interest in this study range from $0.1 \le l_0/L_0 \le 0.3$.

An example of the oscillatory plate motion and the resulting fluid response is shown in Fig. 3. The upper plate begins to oscillate at $t=0$, and the tensile force exerted by the fluid on the plate in response to that motion is also sinusoidal, with a phase lag of approximately 90°. The amplitude of the oscillating force reaches a constant value after one cycle, and this rapid approach to a steady value is observed at all frequencies and amplitudes investigated in the present study.

Assuming the amplitude of oscillation of the top endplate is small enough, we expect the fluid response to be governed by linear viscoelasticity. In this case, the oscillating force should exhibit a single predominant frequency equal to the fundamental frequency of the oscillation. The relative magnitudes of higher harmonics indicate the importance of nonlinear effects. The frequency content of the oscillating force is easily examined by computing the Fourier transform of the signal. Figure 4 contains the amplitude of the discrete Fourier transform of the oscillatory data shown in Fig. 3, computed using familiar algorithms (Press et al. 1992). A large peak at $f_1=\omega/2\pi=1.63$ Hz is present at the fundamental frequency, and several smaller peaks are present at higher harmonics, $f_2=3.26$ Hz, $f_3=4.89$ Hz, and $f_5=8.15$ Hz. Although the magnitude of each higher harmonic is less than 10% of the first harmonic, each higher harmonic will contribute to the overall magnitude and transient shape of the measured force. For this PS025 fluid, the amplitude of the force at the fundamental frequency is observed to increase approximately linearly with both increasing driving frequency and increasing amplitude, $l_0$, over the range of interest.

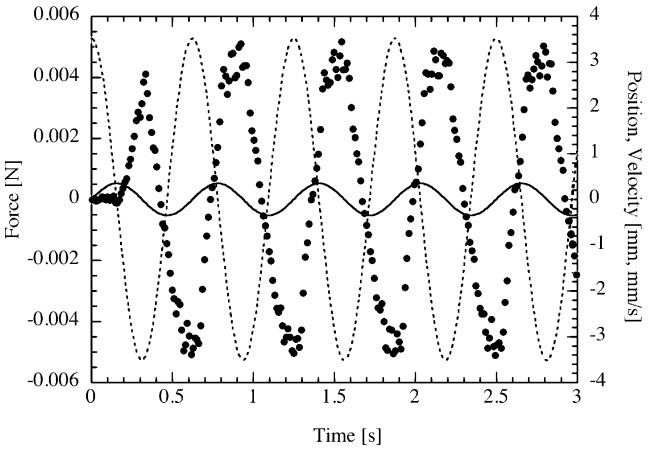


**Fig. 3** Transient response of the tensile force to oscillatory squeeze flow in the filament stretching device ($f_1=1.63$ Hz) for the PS025 fluid. *Solid curve* represents fluctuation of the distance between the two plates about the mean value, $L_0$ (right-hand ordinate); *dashed curve* represents velocity of top plate (also right-hand ordinate). The amplitude of the force oscillation (*filled circle*, shown on the left-hand ordinate) rapidly reaches a steady value, and the response is nearly 90° out of phase with the position oscillation

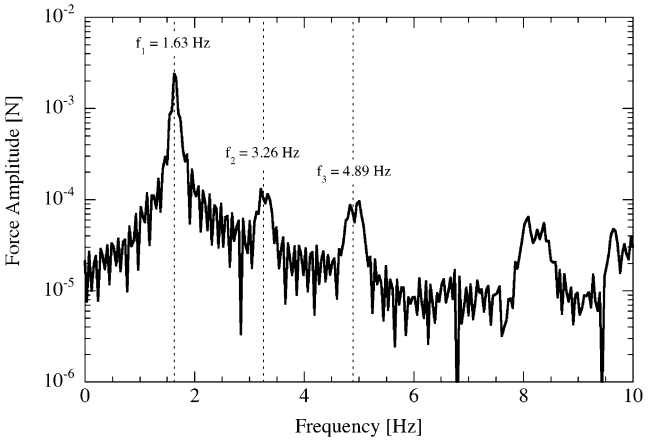


**Fig. 4** Discrete Fourier transform of oscillating tensile force data shown in Fig. 3. While the largest peak corresponds to the fundamental frequency, smaller peaks are evident at several harmonic frequencies, $f_n=nf_1$. The relative magnitudes of the harmonic peaks compared to the fundamental peak indicate the importance of nonlinear viscoelastic effects on the material response

For small-amplitude oscillatory squeeze flow, Phan-Thien and co-workers (Phan-Thien 1980, 1985) have presented several analyses of the flow kinematics and resulting theoretical force response. Field et al. (1996) use this analysis and the principles of deconvolution (Press et al. 1992) to compute the dynamic material functions of viscoelastic liquids after imposing a random squeezing flow. If either the Reynolds number, $\mathrm{Re} = \rho\omega l_0 R_0/\eta_0$, or the aspect ratio, $\Lambda_0 = L_0/R_0$, is small such that $Re\,\Lambda_0 \ll 1$, the velocity field in the squeezing flow can be found using a lubrication approximation. The functional form of the resulting velocity field is identical to that found using a slender filament approximation (Eggers 1993; Eggers and Dupont 1994; Renardy 1994; Spiegelberg et al. 1996), and thus, we expect the analysis of Phan-Thien to be valid for our squeezing flow. In our case, the aspect ratio is $\Lambda_0 = 1.0$, but the Reynolds number is much less than unity, ranging from $0.0073 \le \mathrm{Re} \le 0.29$ for the frequencies of interest in the present study. Using the one-dimensional form of the velocity field resulting from a slender filament approximation, Spiegelberg and co-workers showed that the lubrication solution for the axial velocity in a Newtonian fluid confined between rigid endplates is given by the functional form

$$v_z = \dot{L}_\mathrm{p}(t) g(z,t) \equiv \dot{L}_\mathrm{p}(t)\left(z/L_\mathrm{p}\right)^2\left[3 - 2\left(z/L_\mathrm{p}\right)\right], \qquad (4)$$

where $g$ is a dimensionless function of $z$, the coordinate along the filament axis, and time $t$. The form of Eq. 4 corresponds to a reference frame in which the bottom endplate is held stationary and the top plate accelerates upward at $+\ddot{L}_\mathrm{p}(t)$. The midplane, thus, also accelerates upward at $+\ddot{L}_p(t)/2$. This reference frame corresponds to

that of our filament stretching apparatus and is one of three configurations analyzed by Szabo and McKinley (2003). Differentiating Eq. 4 and applying mass continuity, we obtain the rate-of-strain tensor,

$$\begin{aligned}\dot{\gamma}_{rr} &= \dot{\gamma}_{\theta\theta} = -3\,\dot{E}(t)\left(z/L_p\right)\left[1-\left(z/L_p\right)\right]\\ \dot{\gamma}_{zz} &= -2\,\dot{\gamma}_{rr}\\ \dot{\gamma}_{rz} &= 6\,\dot{E}(t)\left(r/L_p\right)\left[\left(z/L_p\right)-\tfrac{1}{2}\right]\end{aligned}, \tag{5}$$

where $\dot{E}(t)$ is a characteristic strain rate computed from Eq. 2,

$$\dot{E}(t) = \frac{\dot{L}_{\mathrm{p}}(t)}{L_{\mathrm{p}}(t)} = \frac{\omega l_0 \cos\omega t}{L_0 + l_0 \sin\omega t}. \tag{6}$$

We note that the mean value of the strain rate is zero, and the functional form is not significantly different from a pure cosine function, as the quantity in the denominator is nearly equal to unity (in our experiments, $l_0/L_0 = 0.1$). Equation 5 shows that the maximum stretch rate occurs at the midplane, $z = L_{\mathrm{p}}/2$, of the cylindrical fluid sample, where

$$\dot{\varepsilon}_{\|,\max} \equiv \dot{\gamma}_{zz}\left(z = L_{\mathrm{p}}/2\right) = \tfrac{3}{2}\dot{E}(t). \tag{7}$$

We estimate the amplitude of the characteristic stretch rate from Eq. 6 and define a dimensionless strain amplitude, $\gamma_0 \equiv l_0/L_0$, and a dimensionless frequency, or Deborah number, $\mathrm{De}_{\|}$, for the oscillatory squeeze flow,

$$\mathrm{De}_{\|} = \lambda_Z \omega. \tag{8}$$

Applying the momentum equations and integrating over the cross-sectional area of the fluid filament, Phan-Thien found that the oscillatory tensile force is given by

$$F(t) = -\frac{3}{2}\frac{\pi R_0^4}{L_0^3}\eta^*\dot{L}_p(t), \tag{9}$$

where $\eta^*$ is the complex viscosity of the fluid, given by

$$\eta^* = \eta' - i\eta'' = \left|\eta^*\right| e^{-i\Phi}. \tag{10}$$

The magnitude and phase of the complex viscosity are related to the real and imaginary components according to

$$\begin{aligned}\left|\eta^*\right| &= \sqrt{(\eta')^2+(\eta'')^2}\\ \Phi &= \tan^{-1}(\eta''/\eta')\end{aligned}, \tag{11}$$

and $\eta'(\omega)$ and $\eta''(\omega)$ are the same dynamic material functions measured in small amplitude oscillatory shear flow. As $\eta^*$ is complex, we expect the observed transient force to exhibit both in-phase and out-of-phase components relative to the imposed endplate velocity. To obtain a real, time-varying expression for the expected force profile, we first express the position $L_{\mathrm{p}}(t)$ as a complex function,

$$L_p(t) = \mathbb{R}\left\{L_0 - il_0 e^{i\omega t}\right\} \tag{12}$$

where $\mathbb{R}\{\}$ denotes the real component. Differentiating Eq. 12 and substituting into Eq. 9, the resulting real component of the force then becomes

$$F(t) = \frac{3}{2}\frac{\pi R_0^4}{L_0^3}\omega l_0\left|\eta^*\right|\sin(\omega t - \Phi - \pi/2). \tag{13}$$

Thus, the observed transient force is expected to be sinusoidal with a phase lag of $(\pi/2 + \Phi)$ relative to the imposed axial oscillation in the position of the upper plate. By computing the amplitude and phase of the resulting measured force profile, the dynamic material functions can be obtained as functions of the driving frequency, $\omega$.

As shown in Fig. 3, the transient force profile observed in the PS025 fluid behaves, at least qualitatively, as expected from Eq. 13 where we take force to be positive in the $+z$ direction as shown in Fig. 2. Closer inspection of Eq. 11 reveals that $\Phi \approx 0$ if the fluid response is primarily viscous in nature. The measured dynamic shear rheology of the PS025 fluid shown in Fig. 1 is consistent with a dominant viscous response. At low shear rates, both the viscosity and the first normal stress difference are constant and the corresponding linear viscoelastic functions approach consistent limiting values at low frequencies. From this assumption, $\Phi$ is found to increase linearly with frequency in this regime,

$$\Phi \approx \frac{\eta''}{\eta'} = \frac{\Psi_{10}}{2\eta_0}\omega \tag{14}$$

where $\Psi_{10}/2\eta_0 \approx 0.2$s for the PS025 fluid. The viscometric properties of the PS025 fluid measured using conventional shear rheometry techniques are shown in Fig. 1, and we can use measured values from these experiments to estimate that the range of $\Phi$ is $0.0013 \le \Phi \le 0.04$ for the frequency range considered in oscillatory squeeze flow. The phase shift $\Phi$ corresponds to a shift along the time axis, given by

$$\Delta t = \frac{\Phi}{\omega} \tag{15}$$

The *maximum* time shift in the range of interest is expected to be $\Delta t$=0.06 s, which is only a few multiples of the sampling rate, $\Delta t_s$=0.012 s, for the experiments. In addition, the calibrated response time of the force transducer is $\Delta t_r$=0.079 s, as measured from the response of the transducer to a step-change in applied force. Even if the force data is deconvolved from the transducer response, the expected value of $\Delta t$ is on the order of the time resolution that can be observed, and thus, we expect it to be difficult to obtain reliable values for this quantity. However, values of the dynamic viscosity, $\left|\eta^*\right| \approx \eta'$, have been computed using

the amplitude of the measured force profiles and Eq. 13. This amplitude is obtained from the fundamental frequency of the Fourier transform. Values of the resulting dynamic viscosity are shown in Fig. 1 and agree with the values measured in a conventional shear rheometer to within experimental error. In this analysis, we have neglected surface effects, as the capillary number (i.e., the ratio of viscous stresses to capillary pressure) is large, $\mathrm{Ca} = \eta_0 V_{z,\max}/\sigma \gg 1$. We have also neglected effects due to nonlinear viscoelasticity, as $\gamma_0 = l_0/L_0 \ll 1$. The changing curvature of the free surface as the upper endplate oscillates about its mean value leads to an additional force correction whose amplitude is expected to be approximately 10% of the measured force.

We have shown in this section that the oscillatory squeeze flow generated by oscillating the upper endplate in a filament stretching rheometer yields a dynamic viscosity for the PS025 fluid that agrees well with values measured in conventional shear rheometry. However, some nonlinear effects are expected to play a role in the force response, as harmonic peaks are observed in the Fourier transform of the measured force response. The oscillatory squeeze flow described here is expected to result in a net overall alignment of the polystyrene chains along the stretching axis of the filament stretching rheometer at times $t = 0, 2\pi n/\omega$ when the plate passes through its initial position with velocity $v_{z,\max} = \omega l_0$ and extension rate $\dot{\varepsilon}_{\max} \approx 3\omega l_0/2L_0$. In the section entitled "Effect of pre-shear on transient extensional viscosity", we will investigate the effect of this initial alignment on the transient stress growth in a filament stretching experiment.

## Rotational pre-shearing orthogonal to direction of stretching

To generate a steady shear flow in which the principal flow direction is orthogonal to the direction of stretching, the upper endplate of the filament stretching rheometer is rotated using a DC motor that is mounted on the upper translation stage of the device and thus moves along with the upper endplate during a filament stretching experiment. The DC motor is mounted with its rotation axis parallel to the direction of stretching and is then coupled to the upper endplate through a series of gears that translate the rotation of the motor into rotation of the upper endplate about the axial stretching direction. The configuration of the DC motor and associated gearing enables the rotation rate to be controlled in the range of $1.5 \leq \Omega \leq 30$ rad/s by the voltage applied to the DC motor. The resulting rotation rate depends linearly on the applied voltage and is measured using a US digital rotary encoder connected to the data acquisition system that controls the filament stretching device. For the PS025 fluid, the relationship between the voltage (in V) and the rotation rate (in rad/s) is given by $\Omega = 2.53\,V - 1.28$.

Steady torsional shear flow between two rigid circular disks with $R_0 \gg L_0$ is a common configuration in conventional shear rheometry and has been analyzed in detail elsewhere (Bird et al. 1987a). The flow is principally in the azimuthal direction, and the velocity field in the limit $Re \ll 1$ is given by

$$\begin{aligned} v_r &= 0 \\ v_\theta &= \frac{\Omega r z}{L_0} \\ v_z &= 0 \end{aligned} \tag{16}$$

The resulting rate-of-strain tensor is

$$\dot{\gamma} = \begin{bmatrix} 0 & 0 & 0 \\ 0 & 0 & \dot{\gamma}_R r/R_0 \\ 0 & \dot{\gamma}_R r/R_0 & 0 \end{bmatrix} \tag{17}$$

and thus, the shear rate is not constant throughout the fluid sample but rather varies linearly with radial position. The characteristic shear rate, $\dot{\gamma}_R$, is taken at the edge of the disks and is given by

$$\dot{\gamma}_R = \frac{\Omega R_0}{L_0}. \tag{18}$$

Thus, the *dimensionless* shear rate, or Weissenberg number, is defined as

$$\mathrm{Wi}_\perp = \lambda_Z \Omega R_0/L_0. \tag{19}$$

The first normal stress coefficient $\Psi_1$ can be obtained from normal force measurements using the relationship (Bird et al. 1987a)

$$\Psi_1(\dot{\gamma}_R) - \Psi_2(\dot{\gamma}_R) = \frac{\left(F/\pi R_0^2\right)}{\dot{\gamma}_R^2}\left[2 + \frac{d\ln\left(F/\pi R_0^2\right)}{d\ln\dot{\gamma}_R}\right]. \tag{20}$$

The second normal stress coefficient, $\Psi_2(\dot{\gamma}_R)$, is much smaller than $\Psi_1(\dot{\gamma}_R)$ for dilute polymer solutions (Magda et al. 1991), and for the purposes of this analysis, we assume $\Psi_2(\dot{\gamma}_R) \approx 0$.

To obtain $\Psi_1(\dot{\gamma}_R)$, the transient tensile force is measured over a range of rotation rates $\Omega$. Steady values of $F$ are extracted after steady state is reached ($\Delta t \geq 10\lambda_Z \simeq 39$s), and the resulting measurements of $\ln\left(F/\pi R_0^2\right)$ are regressed to a low-order polynomial function. The resulting polynomial is differentiated to obtain the slope given by the second term in Eq. 20. The maximum value of this slope is $d\ln\left(F/\pi R_0^2\right)/d\ln\dot{\gamma}_R = 2$, corresponding to a first normal stress coefficient that is constant with respect to shear rate. Values of $\Psi_1(\dot{\gamma}_R)$ computed using the method described here are shown in Fig. 1, and these values agree reasonably well with normal force measurements from a conventional rheometer. All values $\Psi_1(\dot{\gamma}_R)$ shown in Fig. 1 correspond to measured force values above the resolution of the force

transducer ($\Delta F_{min} \approx 4.5$ mg). However, at the lowest shear rate, the corresponding force is relatively close to the minimum value ($\Delta F \approx 3\Delta F_{min}$), so the errors on this point are expected to be large. We note that some of the error associated with our measurements is due to the relatively large aspect ratio ($\Lambda_0 = 1.0$) as compared with the very low values ($\Lambda_0 \ll 1$) that are typical in conventional parallel plate measurements.

At larger shear rates, the steady torsional shear flow of viscoelastic fluids between two disks becomes unstable, exhibiting a "spiral instability" described and characterized elsewhere (Byars et al. 1994; Rothstein and McKinley 2000; Calado et al. 2005). For the PS025 fluid, the instability is observed for $\dot{\gamma}_R \geq 16.0\,s^{-1}$ and is characterized by a transient force profile that grows erratically and does not reach a steady value in finite time. Sample transient tensile force profiles are given in Fig. 5 for a range of shear rates. For transient shear flow, the relationship between $\Psi_1$ and $\dot{\gamma}_R$ is more complicated than that given in Eq. 20 for steady shear flow. However, the transient force profiles shown in Fig. 5 have been converted into $\Psi_1(t, \dot{\gamma}_R)$ profiles using the same procedure described above for steady shear data, using the same value of $d\ln\left(F/\pi R_0^2\right)/d\ln\dot{\gamma}_R$ that was obtained from steady shear measurements. This procedure allows a direct comparison with transient profiles measured in a conventional rheometer using a cone-and-plate fixture, and Fig. 5 demonstrates that the trends observed in each device are consistent. Although the initial overshoot in the normal force is larger in the cone-and-plate experiment shown here, the steady values of $\Psi_1(t, \dot{\gamma}_R)$ decrease due to shear thinning as expected for both the parallel-plate flow in the filament stretching device and the cone-and-plate flow. A transient force profile for a shear rate above the onset of the spiral instability is also shown in the figure, and at this shear rate, the measured force fluctuates erratically and increases to values well above the expected steady value for that shear rate. A theoretical analysis by Avagliano and Phan-Thien (1996) and experimental results reported by Byars et al. (1994) indicate that the critical shear rate for the onset of the spiral instability should depend linearly on the aspect ratio, $L_0/R_0$. Experimental values of the critical shear rate reported by Byars et al. for similar fluids indicate that the critical shear rate for the PS025 fluid should be approximately $\dot{\gamma}_R \approx 12.3\,s^{-1}$, which is consistent with the observed behavior.

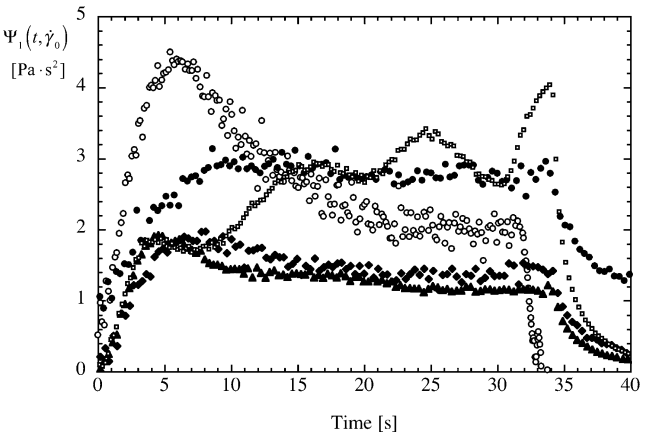


**Fig. 5** Startup and relaxation of normal stresses in the PS025 fluid as measured in rotational shear flow. Steady values of $\Psi_1$ reached in parallel plate flow in the filament stretching device (*filled circle*, 3.4 $s^{-1}$; *filled diamond*, 8.6 $s^{-1}$; *filled triangle*, 15.6 $s^{-1}$) agree with those measured in a conventional cone-and-plate rheometer (*open circle*, 4.68 $s^{-1}$, RMS-800). Torsional flow in the filament stretching device (with aspect ratio $R_0/H = 1.0$) becomes unstable above a critical shear rate of about $\dot{\gamma}_{crit} \approx 16 s^{-1}$ (*open square*, 16.9 $s^{-1}$)

## Effect of pre-shear on transient extensional viscosity

Filament stretching experiments were carried out at a fixed Deborah number, $De \equiv \lambda_z \dot{\varepsilon}_0 \approx 12.5$ where $\dot{\varepsilon}_0$ is the uniaxial extension rate and a range of pre-shear conditions varying the Weissenberg numbers $Wi_\perp$ or the Deborah number $De_\parallel$ and strain amplitude $\gamma_0$. The value of De was chosen to not only minimize effects of sagging due to gravity on the stretching filament (Anna et al. 2001) but also to maximize the Hencky strain $\varepsilon = \dot{\varepsilon}_0 t = \ln(L/L_0)$ achievable within the physical limits of the rheometer. At this Deborah number, a final Hencky strain of $\varepsilon_f \approx 5.6$ is realized, allowing the transient tensile stresses to approach a steady state value. The values of $Wi_\perp$ and $De_\parallel$ span the range achievable in the apparatus. Pre-rotation of the top plate is imposed for 30 s ($\dot{\gamma}t \geq 80, t/\lambda_z \approx 7.7$) before stretching to allow the stresses to reach a steady value. Pre-oscillation is imposed for the same duration, corresponding to three cycles at the lowest applied frequency, $\omega$=0.63 Hz, and 75 cycles at the highest applied frequency, $\omega$=15.7 Hz. The initial aspect ratio of the fluid filament was fixed at $\Lambda_0 = L_0/R_0 = 1.0$.

An open-loop control algorithm described previously (Anna et al. 1999; Orr and Sridhar 1999) is used for the experiments presented here to generate a nearly ideal uniaxial elongational flow in which the diameter at the midpoint of the filament decreases exponentially with one half the nominal extension rate $\dot{\varepsilon}_0$. Because the variation in the resulting diameter profiles is independent of the Weissenberg number imposed in pre-shear, identical motion profiles were used during the stretching portion of the experiment in order to eliminate uncertainties due to the kinematics. In all experiments presented here, the desired elongation rate is $\dot{\varepsilon}_0 = 3.0\,s^{-1}$. For the filament stretching experiments with oscillatory pre-shearing, the average actual elongation rate realized is $\dot{\varepsilon}_{act} = 2.95 \pm 0.05\,s^{-1}$, which agrees with the programmed rate to within experi-

mental error. The resulting Deborah number is De=12.4± 0.5; temperature fluctuations between experiments lead to a larger percentage error in De. For the filament stretching experiments performed with orthogonal pre-shearing, the average actual elongation rate realized is $\dot{\varepsilon}_{act} = 3.15 \pm 0.06\, s^{-1}$ which agrees with the programmed rate to within 5.0%. The resulting Deborah number for these experiments is De=12.8±0.2.

Previous filament stretching experiments with polystyrene-based Boger fluids (Tirtaatmadja and Sridhar 1993; Gupta et al. 2000; Anna et al. 2001) have shown that the transient stress growth for this class of fluids (with no pre-shear) in uniaxial elongational flow is nearly independent of the elongation rate or Deborah number for $De \geq 5$ (Gupta et al. 2000; Larson 2005). In addition, analysis of experimental deviations shows that transient Trouton ratios obtained from filament stretching experiments performed with identical operating conditions are reproducible to within about 20% (Anna et al. 2001). Thus, any effects arising from pre-deformation of the fluid filament must fall consistently outside this range of expectations in order to be considered significant.

## Oscillatory parallel pre-straining

The evolution in the transient tensile forces is shown in Fig. 6 for selected oscillatory pre-straining experiments. The amplitude of the oscillating force rapidly reaches a steady value, and the magnitude increases with the frequency. The tensile force profiles measured during subsequent stretching show qualitatively similar shapes, but the magnitude of the force at a given time depends on the pre-oscillation frequency. The maximum peak force value corresponds to the lowest frequency reported.

Transient Trouton ratios computed from the raw force data in Fig. 6 are shown in Fig. 7. The shape of these curves is observed to depend weakly on the pre-oscillation

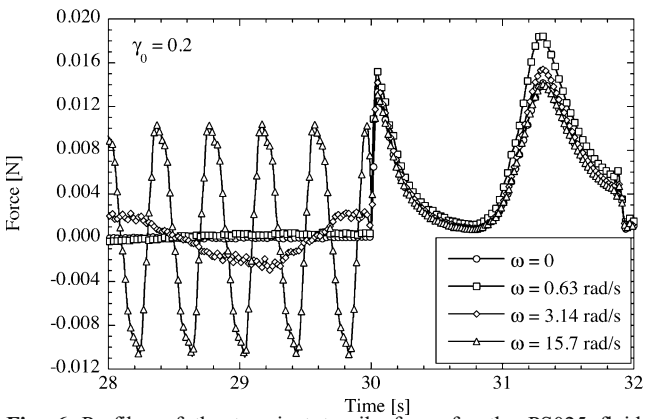


**Fig. 6** Profiles of the transient tensile force for the PS025 fluid measured in the filament stretching device during oscillatory squeeze flow and subsequent stretching. The Deborah number for the stretching portion is fixed at De=12.4, and the oscillation frequency varies

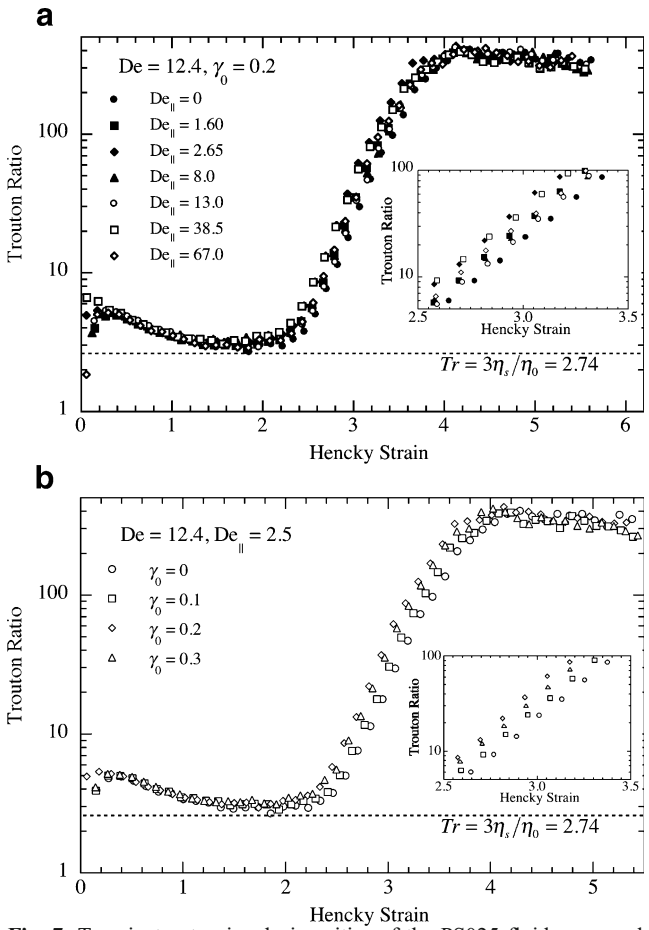


**Fig. 7** Transient extensional viscosities of the PS025 fluid measured in the filament stretching device after pre-straining the fluid using oscillatory squeeze flow. The Deborah number for the stretching portion is fixed at De=12.4. **a** Effect of varying oscillation frequency for fixed $\gamma_0$=0.2 (*filled circle*, $De_{\|}$=0; *filled square*, $De_{\|}$=1.60; *filled diamond*, $De_{\|}$=2.65; *filled triangle*, $De_{\|}$=8.0; *open circle*, $De_{\|}$=13.0; *open square*, $De_{\|}$=38.5; *open diamond*, $De_{\|}$=67.0); and **b** effect of varying amplitude of oscillation at constant frequency of $\omega = 0.63$rad/s ($De_{\|} \cong 2.5$): (*open circle*, $\gamma$=0; *open square*, $\gamma_0$=0.1; *open diamond*, $\gamma_0$=0.2; *open triangle*, $\gamma_0$=0.3). The *insets* show a magnified view of the effect of pre-stretching on the transient stress growth

frequency, as shown in Fig. 7a in which the amplitude of oscillation is fixed at $\gamma_0 = l_0/L_0 = 0.2$ ($l_0$=0.07 cm). At all frequencies $\omega \neq 0$, the rate of stress growth is consistently accelerated relative to the no pre-shear case, although the stresses approach the same steady-state value at large Hencky strains. The dependence of the strain hardening behavior on frequency appears to be non-monotonic. At the lowest $De_{\|}$, the PS025 fluid strain hardens significantly faster than it does in the case of no pre-shearing, whereas the strain hardening is not accelerated as much for the larger $De_{\|}$ values. As shown in the inset of Fig. 7(a), at a Hencky strain of $\varepsilon$=3, the extensional viscosity is 150% larger for $De_{\|} \approx 2.5$ than for $De_{\|}$=0, although the corresponding increase is only 25% for $De_{\|}$=13.0. Viewed in an alternate way, the strain hardening is accelerated by a

maximum of approximately $\Delta\varepsilon \approx 0.25$ for $De_{\|}$=2.65 compared with $De_{\|}$=0. At larger frequencies, the observed enhancement in the strain hardening is small enough to nearly fall within experimental errors, and so the trend at these frequencies is not clear.

On the other hand, Fig. 7b shows that increasing the amplitude of oscillation $\gamma_0$ at a low frequency, $\omega$=0.63 rad/s (nominally $De_{\|} = 2.46$), consistently increases the rate of strain hardening. The inset of Fig. 7b shows that for $\gamma_0$=0.2 the degree of enhancement in the strain hardening is similar to that shown in Fig. 7a. At a Hencky strain of $\varepsilon$=3, the extensional viscosity is 150% larger than the value corresponding to $\{De_{\|} = 0, \gamma_0=0\}$, and the strain hardening is accelerated by approximately $\Delta\varepsilon \approx 0.2$ strain units compared with $\{De_{\|} = 0, \gamma_0=0\}$. The results shown in both Fig. 7a and b can be compared with other results predicting modifications to the extensional stress growth. For example, Li and Larson (2000) show a significantly greater advancement in the stress growth, corresponding to $\Delta\varepsilon \approx 1.0$, when the solvent is a good solvent for the polymer chains rather than a theta solvent. A good solvent is expected to lead to an initially expanded configuration in the polymer chain, which is expected to lead to a faster approach to steady-state extension. Similarly, in our case, oscillation parallel to the axis of subsequent stretching orients the polymer chains along the direction of stretching, allowing a faster approach to full extension of the chains. The effect is maximized at *lower* frequencies and larger oscillation amplitudes, as the period of oscillation at these frequencies is on the order of the fluid relaxation time, $2\pi/\omega \approx \lambda$. At higher frequencies, the fluid cannot respond sufficiently rapidly to the flow, leading to a decreased magnitude of pre-orientation in the polymer chains before stretching. In the section entitled "Modeling pre-shear effects", we will examine the trends predicted from the FENE-P constitutive model and compare these to our experimental observations.

## Steady orthogonal pre-shearing

During orthogonal shearing, the normal force has the opposite sign to the tensile force during stretching, as shown in Fig. 8. The complete force balance on the fluid column now contains several other components of the stress tensor in addition to the radially averaged principal stress difference, $<\tau_{zz}-\tau_{rr}>$. The complete balance of stresses in the filament accounting for these terms along with gravity and surface tension is given by Szabo (Szabo 1997; Szabo and McKinley 2003),

$$\langle \tau_{zz} - \tau_{rr} \rangle + \frac{1}{2}\langle \tau_{rr} - \tau_{\theta\theta} \rangle + \frac{1}{2}\langle r\tau_{zr} \rangle' = \frac{F_p + (\rho g V_0 - \pi\sigma D_{mid})/2}{\pi (D_{mid}/2)^2} \quad (21)$$

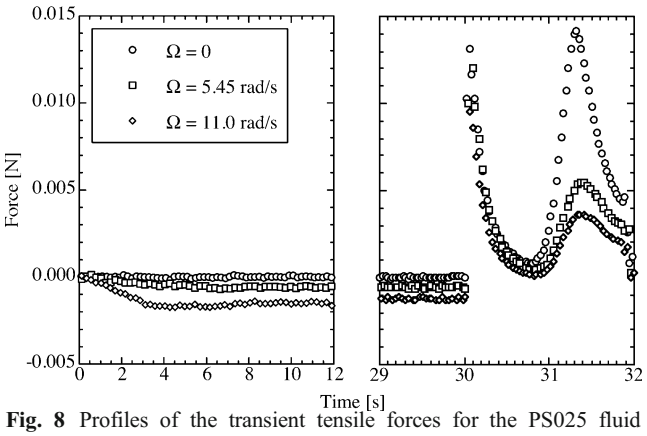


**Fig. 8** Profiles of the transient tensile forces for the PS025 fluid measured in the filament stretching device after pre-shearing the fluid using steady torsional flow. The Deborah number for the stretching portion is fixed at De=12.8, and the rotation rate is varied

where $\langle\rangle$ denotes a radially averaged quantity, the prime on the $\tau_{zr}$ term denotes an axial derivative, $V_0 = \pi L_0 (D_0/2)^2$ is the volume of the fluid sample, $\sigma$ is the surface tension of the fluid, and $\rho$ is the density of the fluid. In ideal uniaxial extension, with no pre-shearing, Eq. 21 simplifies considerably, and the transient extensional viscosity is calculated from

$$\mathrm{Tr} = \frac{\overline{\eta}^{+}(t,\dot{\varepsilon}_0)}{\eta_0} = \frac{[\tau_{zz}(t) - \tau_{rr}(t)]}{\eta_0 \dot{\varepsilon}_0} = \frac{F_p}{\pi (\mathrm{D_{mid}}/2)^2 \eta_0 \dot{\varepsilon}_0} \quad (22)$$

However, when a pre-shearing deformation has been imposed, the relative contributions of the terms on the left-hand side of Eq. 21 cannot be determined from a single observable, $F_p(t)$, and thus, the *apparent* transient extensional viscosity computed using Eq. 22 is not the true extensional viscosity, but instead incorporates all of the stress components in Eq. 21. It is this memory of previous shearing deformations that complicates analysis of spinline data and other steady Eulerian elongational flows in which boundary conditions on the tensile stresses are required (Petrie 1995; Ramanan et al. 1997; Bechtel et al. 2001).

The effect of orthogonal steady pre-shearing shown in Fig. 9 is opposite to that observed in parallel oscillatory pre-straining. In this case, the strain hardening in the PS025 fluid is significantly delayed as a result of the orthogonal pre-shearing. The delay in strain hardening increases and the apparent steady state plateau value of the Trouton ratio decreases nearly monotonically as the rotation rate increases. For example, at a Hencky strain of $\varepsilon$=3, the transient extensional viscosity is 66% lower for $\mathrm{Wi}_{\perp}$=53.6 than for $\mathrm{Wi}_{\perp}$=0. The magnitude of the delay in the Hencky strain reaches a maximum of approximately $\Delta\varepsilon \approx 0.5$ at $\mathrm{Wi}_{\perp}$=53.6. This delay is greater than the maximum enhancement of $\Delta\varepsilon \approx 0.2$ due to oscillatory pre-stretching, but still not as great as the enhancement of $\Delta\varepsilon \approx 1.0$ due to

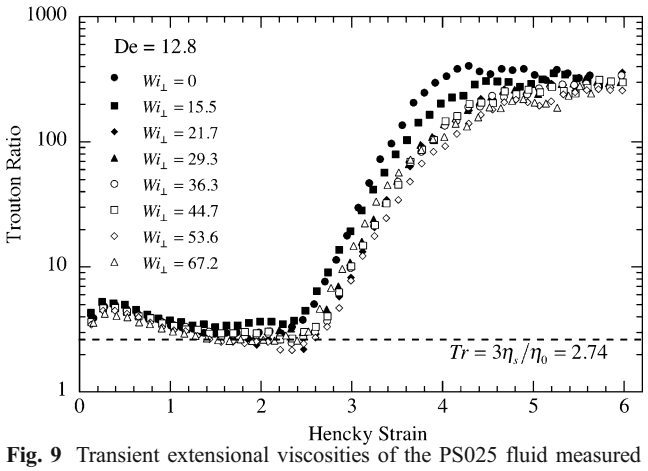


**Fig. 9** Transient extensional viscosities of the PS025 fluid measured in the filament stretching device after pre-shearing the fluid using steady torsional flow. The Deborah number for the stretching portion is fixed at De=12.8, and the rotation rate is varied (*filled circle*, $Wi_\perp$=0; *filled square*, $Wi_\perp$=15.5; *filled diamond*, $Wi_\perp$=21.7; *filled triangle*, $Wi_\perp$=29.3; *open circle*, $Wi_\perp$=36.3; *open square*, $Wi_\perp$=44.7; *open diamond*, $Wi_\perp$=53.6; *open triangle*, $Wi_\perp$=67.2)

solvent quality that was observed in the Brownian dynamics simulations of Li and Larson (2000).

It is worth noting that the actual steady-state value of the Trouton ratio may not have been realized at the maximum Hencky strain observed in the experiments. The true steady-state Trouton ratio, corresponding to full extension of the polymer chains, is expected to be independent of pre-shear rate, but this value may not be achieved until significantly larger Hencky strains ($\varepsilon$>6.5) have been reached (Gupta et al. 2000). In the present experiments, the value of the Trouton ratio at $\varepsilon \approx 6$ is $Tr = 277 \pm 47$.

At the highest applied rotation rate shown in Fig. 9, the spiral instability discussed earlier is observed (cf. Fig. 5). Before the onset of this elastic instability, the delay in strain hardening monotonically increases with the pre-shear rate (and with $Wi_\perp$), but above a critical rate, this delay is reduced. Experimental and numerical observations have shown that the spiral elastic instability is characterized by secondary "roll cells" in which fluid elements follow toroidal paths about the principal flow direction (Byars et al. 1994; Avagliano and Phan-Thien 1996, 1999). A plausible rationalization for the reduced delay in tensile stress growth during stretching subsequent to an unstable torsional flow is found by considering the orientation of the polymer chains in such a flow. The three-dimensional time-dependent flow that develops after onset of instability implies that the polymer chains may no longer be oriented principally along the primary (tangential) flow direction. As a result, the net orientation of the polymer chains orthogonal to the stretching direction is reduced, and consequently, a somewhat reduced Hencky strain is needed to achieve fully stretched polymer chains during stretching. We note, however, that at the highest rotation rate the Hencky strain needed for a given level of strain hardening to be attained is still larger than that required when no pre-shearing has occurred.

## Modeling pre-shear effects

In this section, we use the FENE-P dumbbell model (Bird et al. 1987b) to evaluate the effects of parallel oscillatory pre-straining and orthogonal rotational pre-shearing on the transient stress growth in a slender fluid filament subject to uniaxial extensional flow. We select this model, rather than more accurate bead-spring models that have been shown to capture quantitatively the transient stress growth in uniaxial elongation without pre-shearing, because it is the simplest canonical model for a dilute polymer solution and because it represents the level of description employed in most complex flow simulations and polymeric drag reduction studies (Massah et al. 1993; Dubief et al. 2004; Stone et al. 2004; Dimitropoulos et al. 2005; Housiadas et al. 2005). It is worth noting in particular that we have not considered the influence of conformation-dependent drag in our choice of constitutive models, although this effect has been shown to play an important role in determining the effect of deformation history close to the coil–stretch transition (Beck and Shaqfeh 2006; Prabhakar and Prakash 2006; Prabhakar et al. 2006; Hoffman and Shaqfeh 2007). We seek to determine whether single-mode dumbbell models can capture the qualitative features observed in filament stretching experiments with a pre-shear step. The FENE-P model is described by a set of evolution equations for the dimensionless configuration tensor $\mathbf{A} = \langle \underline{\mathbf{R}}\,\underline{\mathbf{R}} \rangle$ describing the ensemble average of the FENE dumbbell orientations, given by

$$\lambda_1 \, \mathbf{A}_{(1)} = \mathbf{I} - f(\mathrm{tr}\mathbf{A})A \qquad (23)$$
$$f(\mathrm{tr}\mathbf{A}) = \left[\frac{1}{1 - \mathrm{tr}\mathbf{A}/L^2}\right]$$

where $\lambda_1$ is the longest relaxation time, and $L$ is the finite extensibility of the dumbbell. The stresses in a FENE-P fluid are then given by

$$\boldsymbol{\tau}_\mathrm{p} = \tfrac{\eta_\mathrm{p}}{\lambda_1}[f(tr\mathbf{A})\mathbf{A} - \mathbf{I}] \qquad (24)$$
$$\boldsymbol{\tau} = \boldsymbol{\tau}_\mathrm{p} + \boldsymbol{\tau}_\mathbf{s}$$

where $\boldsymbol{\tau}_\mathrm{p}$ is the polymeric contribution to the stress, and $\boldsymbol{\tau}_s = \eta_s\dot{\gamma}$ is the solvent contribution. For both types of pre-shearing, the evolution equations are simplified for the particular velocity field imposed before stretching, and the equations are then integrated at each time step using

standard routines for stiff ordinary differential equations (ODEs). The accumulated stress in the filament at the instant when shearing ceases and stretching begins is then used as the initial condition for the purely uniaxial elongational flow. For the PS025 fluid, the finite extensibility is $L$=93, and we use the longest relaxation time obtained from the Zimm spectrum for $\lambda_1$.

Parallel oscillatory pre-straining

In the case of oscillatory squeeze flow, we know from the analysis of Phan-Thien (1980) and from the slender filament approximation that the velocity field follows the lubrication solution given in Eq. 4. Equation 5 shows that the components of the rate-of-strain tensor depend, in general, on both the radial and axial positions. To simplify the model calculation, we focus our attention on the axial midplane ($z = L_p/2$) of the fluid filament. At this location, the velocity field is purely extensional, and the elongation rate is a maximum, leading to the maximum orientation of the FENE dumbbells within the fluid filament. At the axial mid-plane of the filament, the rate-of-strain tensor is

$$\dot{\gamma}\left(z = L_p/2\right) = \begin{bmatrix} -\frac{3}{2}\dot{E}(t) & 0 & 0 \\ 0 & -\frac{3}{2}\dot{E}(t) & 0 \\ 0 & 0 & +3\dot{E}(t) \end{bmatrix} \qquad (25)$$

Now, the components of the evolution equations for the polymeric stretch have the identical form to that of an ideal uniaxial extensional flow, with an effective time-varying elongation rate of $\dot{\varepsilon} = \frac{3}{2}\dot{E}(t) \approx (3\omega l_0/2L_0)\cos\omega t$ for $\gamma_0 = l_0/L_0 \ll 1$ (see Eqs. 6 and 7).

We choose oscillatory flow parameters that correspond to the experimental conditions reported in Figs. 7a and b and integrate the evolution equations specialized for the rate-of-strain tensor given in Eq. 6 from $t$=0 to $t=t_1$=30 s ($t_1/\lambda_1 = 7.7$). As observed in the experimental force profiles, the computed tensile stresses rapidly reach steady state amplitude during the oscillatory flow. At time $t=t_1$, the components of the orientation tensor **A** are extracted and used as initial conditions to begin solving the evolution equations for ideal uniaxial extensional flow. The uniaxial extensional flow is solved for a Deborah number of De= 12.4, corresponding to the experimental conditions, up to a final Hencky strain of $\varepsilon_f$=6.0. The resulting transient Trouton ratio profiles are shown in Figs. 10a,b.

The effects of increasing oscillation frequency as predicted by the FENE-P model are shown in Fig. 10a, and the trends observed are nearly identical to those observed experimentally. For all $De_{||}$>0, the strain hardening of the FENE chains is enhanced and, as observed

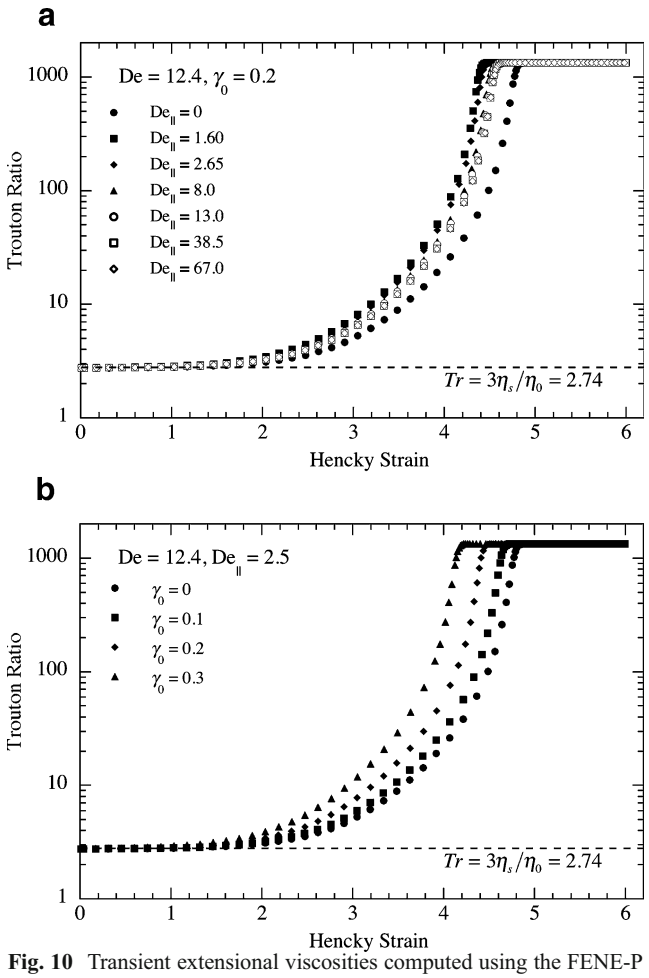


**Fig. 10** Transient extensional viscosities computed using the FENE-P model after application of an oscillatory squeeze flow. The fluid parameters correspond to the PS025 fluid, and the Deborah number for the stretching portion is fixed at De=12.4. **a** Effect of varying the oscillation frequency for fixed $\gamma_0$=0.2 (*filled circle*, $De_{||}$=0; *filled square*, $De_{||}$=1.60; *filled diamond*, $De_{||}$=2.65; *filled triangle*, $De_{||}$=8.0; *open circle*, $De_{||}$=13.0; *open square*, $De_{||}$=38.5; *open diamond*, $De_{||}$= 67.0); and **b** effect of varying amplitude of oscillation for fixed $De_{||} \cong$ 2.5 (*filled circle*, $\gamma_0$=0; *filled square*, $\gamma_0$=0.1; *filled diamond*, $\gamma_0$=0.2; *filled triangle*, $\gamma_0$=0.3)

experimentally, the enhancement does not vary monotonically with $De_{||}$. The most pronounced shift occurs at the lowest Deborah number, $De_{||}$ = 1.6, and the resulting extensional viscosity is 50% larger at a Hencky strain of $\varepsilon$= 3. As observed experimentally, the enhancement decreases as the oscillation frequency increases. At large $De_{||}$, the transient Trouton ratio becomes independent of $De_{||}$, although in this limiting case, there is still enhancement of strain hardening compared with $De_{||} = 0$.

The non-monotonic dependence of the enhancement in strain hardening on oscillation frequency, including the non-zero shift in the high frequency limit, may be rationalized by considering the linear viscoelastic response of the PS025 fluid. Recall that we have selected sufficiently

small oscillation amplitudes during pre-stretching such that the material response is expected to be linear. A comparison of material functions measured from both dynamic shear and extensional flows supports this assumption (see Fig. 1). At high frequencies, the fluid response is predominantly elastic, and thus, the polymeric fluid stresses are *in phase* with the oscillatory strain. In other words, in the "elastic limit" $De_{\|} \gg 1$, the chains experience neo-Hookean deformation that depends only on strain and not on strain rate. At lower frequencies, on the other hand, the fluid response is primarily viscous, and the fluid stresses are out of phase with the oscillatory strain. Thus, we expect that the stress growth during subsequent stretching can be predicted based purely on the known deformation of the chains at $t = 0, 2\pi n/\omega, \ldots$ when the oscillating plate passes through the midpoint of its trajectory. To test this hypothesis, we examine values of the components of the orientation tensor **A** at the end of the oscillatory pre-stretching, but just before exponential stretching. The difference between the axial and radial diagonal components at $t=0$, denoted $(A_{zz} - A_{rr})_0$, represents the magnitude of the initial stretch in the polymer chains along the axis of the filament. Figure 11 shows the dependence of this quantity on $\mathrm{De}_{\|}$ for three different values of the oscillation amplitude, $\gamma_0$. We see that the degree of stretching of the polymer chains reaches a maximum at *moderate* $De_{\|} \approx 1$ , but that the chain stretch is reduced at oscillatory frequencies that are either above or below this value. As the oscillation amplitude $\gamma_0$ increases, the degree of stretching also increases, further magnifying the peak in the pre-stretch value at moderate $\mathrm{De}_{\|}$. Consistent with earlier physical arguments, we see that in the high frequency elastic limit, the quantity $(A_{zz} - A_{rr})_0$ approaches zero when the oscillating plate passes through the midpoint of its trajectory. However, at lower frequencies, even as the oscillation amplitude decreases toward zero, we observe a finite, positive value of $(A_{zz} - A_{rr})_0$.

The observed pre-stretch of the molecules computed in terms of $(A_{zz} - A_{rr})_0$ can be estimated analytically by considering the evolution equation at the axial midplane of the filament where the deformation is purely elongational and the elongation rate and orientation of the FENE dumbbells are at a maximum. We specialize the evolution equation given in Eq. 23 for the rate-of-strain tensor given in Eq. 25 and assume small perturbations on the initial values of the components of **A**, such that $A_{rr} \approx 1+\varepsilon_{rr}$ and $A_{zz} \approx 1+\varepsilon_{zz}$, where $\varepsilon_{rr} \ll 1$ and $\varepsilon_{zz} \ll 1$. In this limit, we obtain the dimensionless evolution equations:

$$\begin{aligned} \frac{\partial A_{zz}}{\partial t} + \left(1 + 6\gamma_0 \mathrm{De}_{\|} \cos\left(\mathrm{De}_{\|}\bar{t}\right)\right) A_{zz} &= 1 \\ \frac{\partial A_{rr}}{\partial t} + \left(1 + 3\gamma_0 \mathrm{De}_{\|} \cos\left(\mathrm{De}_{\|}\bar{t}\right)\right) A_{rr} &= 1 \end{aligned} \tag{26}$$

where $\bar{t} \equiv t/\lambda_z$ is the dimensionless time. We seek a perturbation solution of the form $A \approx 1 + De\, Z_1(\bar{t}) + De^2\, Z_2(\bar{t}) + \mathrm{O}\left(De^3\right)$ for each component and obtain the first-order approximate solution

$$\begin{aligned} A_{zz} &\approx 1 - \left[\frac{6\gamma_0 \mathrm{De}_{\|}}{\left(1+\mathrm{De}_{\|}^2\right)} + 1\right] e^{-\bar{t}} + \frac{6\gamma_0 \mathrm{De}_{\|}}{\left(1+\mathrm{De}_{\|}^2\right)} \left[\cos\left(\mathrm{De}_{\|}\bar{t}\right) + \mathrm{De}_{\|} \sin\left(\mathrm{De}_{\|}\bar{t}\right)\right] \\ A_{rr} &\approx 1 - \left[\frac{3\gamma_0 \mathrm{De}_{\|}}{\left(1+\mathrm{De}_{\|}^2\right)} - 1\right] e^{-\bar{t}} + \frac{3\gamma_0 \mathrm{De}_{\|}}{\left(1+\mathrm{De}_{\|}^2\right)} \left[\cos\left(\mathrm{De}_{\|}\bar{t}\right) + \mathrm{De}_{\|} \sin\left(\mathrm{De}_{\|}\bar{t}\right)\right] \end{aligned} \tag{27}$$

The second term in each expression represents the initial viscoelastic transient response of the dumbbells, which decays after many cycles leaving an oscillatory response in $(A_{zz} - A_{rr})_0$ with phase angle and magnitude that vary with $\mathrm{De}_{\|}$. The amplitude of this initial elongational deformation evaluated at time $t/\lambda_z = 2n\pi/De_{\|}$, corresponding to an integer multiple of cycles of oscillatory squeeze flow, is approximately

$$(A_{zz} - A_{rr})_0 \approx \frac{9\gamma_0\, De_{\|}}{\left(1 + De_{\|}^2\right)}. \tag{28}$$

This function goes through a maximum at $\mathrm{De}_{\|}=1$, and the magnitude increases linearly with the strain amplitude. The results of this first-order estimate are compared with the values computed via the FENE-P model in Fig. 11. The agreement between computed and approximate values is reasonably good at small strain amplitude, $\gamma_0=0.1$, but the asymptotic expression is less accurate at higher values of the strain amplitude. This is because of the strongly nonlinear and asymmetric variation in the oscillatory extension rate imposed during the pre-straining (cf.

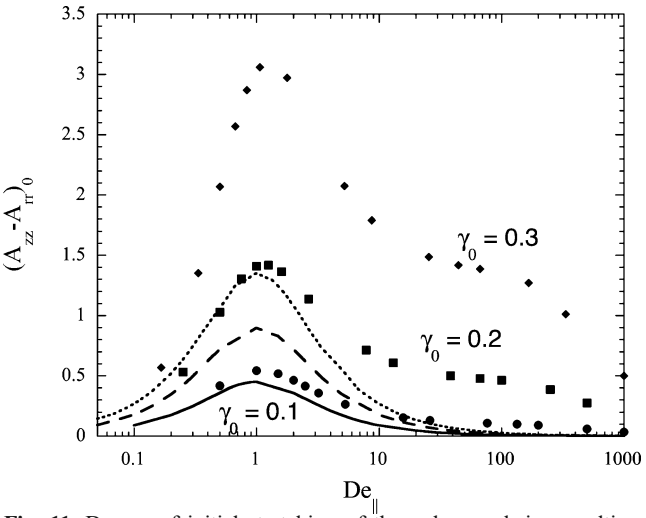


**Fig. 11** Degree of initial stretching of the polymer chains resulting from an oscillatory squeezing flow applied just before filament stretching, as computed from a FENE-P model. The difference between the axial and radial components of the orientation tensor **A** monotonically increases as the amplitude of oscillation increases, but exhibits non-monotonic behavior as the Deborah number increases

Eq. 6) which gives rise to higher harmonic terms in the solution of Eqs. 26. Nevertheless, the analytical expression demonstrates that a finite pre-stretch of the polymer chains is possible even when the initial pre-straining motion is in the linear viscoelastic regime.

Increasing the amplitude of oscillation also has a pronounced effect on the predicted transient extensional viscosity. Figure 10b shows the result of increasing the oscillation amplitude while keeping the oscillation frequency fixed at a low applied value of $\omega$=0.63 Hz (corresponding to $De_{\|} = \lambda_1\omega = 2.5$). As the amplitude increases, the rate of extensional stress growth significantly increases, and the magnitude of this effect is even greater than is observed in the experiments. A larger oscillation amplitude increases the deformation of the liquid bridge between the plates of the rheometer, increasing the overall orientation of the polymer chains. In addition, at higher amplitudes, nonlinear elasticity will play an increasingly important role, possibly leading to some strain hardening during the oscillatory flow regime itself. It is important to note that the steady-state Trouton ratio is identical for all filament stretching experiments, independent of the initial oscillatory flow conditions.

## Orthogonal rotational pre-shearing

In the case of steady shearing flow between two parallel disks, we specialize the evolution equations for the FENE-P model to correspond to the rate-of-strain tensor in Eq. 17. In addition, we assume the following form for the stress tensor:

$$\boldsymbol{\tau} = \begin{bmatrix} \tau_{rr} & 0 & 0 \\ 0 & \tau_{\theta\theta} & \tau_{\theta z} \\ 0 & \tau_{\theta z} & \tau_{zz} \end{bmatrix} \tag{29}$$

The *rr*- and *zz*- components of the stress tensor are zero, as the second normal stress coefficient $\psi_2$ is zero for the FENE-P model. The problem is further simplified by assuming the fluid stresses have reached steady values so that the time derivatives in the evolution equations can be assumed to be zero. The result of this assumption is a set of algebraic equations for the steady-state components of the orientation tensor **A**, given by

$$\begin{aligned} -2\lambda_Z\dot{\gamma}_R\tfrac{r}{R_0}A_{\theta z} &= 1 - fA_{\theta\theta} \\ 0 &= 1 - fA_{zz} \\ -\lambda_Z\dot{\gamma}_R\tfrac{r}{R_0}A_{zz} &= -fA_{\theta z} \\ A_{zz} &= A_{rr} \end{aligned}, \tag{30}$$

where $f$=$f$(tr**A**) is the FENE factor given in Eq. 23, and tr**A**=$A_{\theta\theta}$+2$A_{zz}$. The rate-of-strain tensor given in Eq. 17 is not homogeneous, but depends on the radial position, therefore the components of the orientation tensor and the stress tensor will also depend on the radial position, $A_{ij}(r)$ and $\tau_{ij}(r)$. Thus, Eq. 30 can in general be solved simultaneously at each value of $r$, and the stress distribution $\tau_{ij}(r)$ over the cross-section of the slender filament can be related to $A_{ij}(r)$ by Eq. 24.

The transient tensile stresses in the purely uniaxial elongational flow regime are generally assumed to be uniform over the filament cross-section, and as a result, a single set of quasi-one-dimensional ODEs is integrated for this flow. To use the steady state cross-sectional stress distribution resulting from Eq. 30 to compute initial conditions for the uniaxial extensional flow regime, an appropriate spatial average must be computed, because the force balance given in Eq. 21 requires radially averaged stress distributions, e.g., $\langle\tau_{zz} - \tau_{rr}\rangle$. Consideration of the cross-sectional stress distributions shows that the maximum stresses occur at the outer radius $R_0$ of the disks. Any radial averaging, thus, serves to decrease the magnitude of the effective initial stresses. As a lower effective initial stress only serves to decrease the effect of the pre-shearing flow, we chose to take the maximum stress values for the purposes of this simple illustrative computation. This corresponds to following the annulus of material located at $\{z = 0, R = R_0\}$. More detailed finite element simulations of the entire inhomogeneous flow field with appropriate boundary conditions could yield information about the appropriate average to use to accurately simulate an actual filament stretching experiment with torsional pre-shearing.

As in the case of oscillatory squeezing flow, we choose shearing and elongational flow parameters to correspond to the actual experimental conditions presented in Fig. 9. The identical range of $\mathrm{Wi}_{\perp}$ used in the experiments are applied, and the Deborah number during uniaxial elongation is held fixed at De=12.8. The transient extensional stresses are computed from the evolution equations for purely uniaxial extensional flow as they were for the oscillatory pre-shear case. However, two additional evolution equations must be solved along with the equations for the radial and axial components of the orientation tensor, $A_{rr}$ and $A_{zz}$. As the initial values of $A_{\theta z}$ and $A_{\theta\theta}$ are non-zero, these quantities also evolve over time, and in general, they couple into the evolution of the radial and axial components. As a result, both the principal and the secondary tensile stress differences are initially non-zero and are important in the calculation of the force balance given in Eq. 21.

The results of the calculations described here are shown in Figs. 12a and b. As observed in the experimental measurements, the computed profiles for the transient Trouton ratios are significantly affected by the pre-shearing flow. The principal dimensionless extensional viscosity, or "true" Trouton ratio, based on the principal tensile stress difference, defined in Eq. 22, is shown in Fig. 12a. In this case, the initial and final plateau values of the Trouton ratios

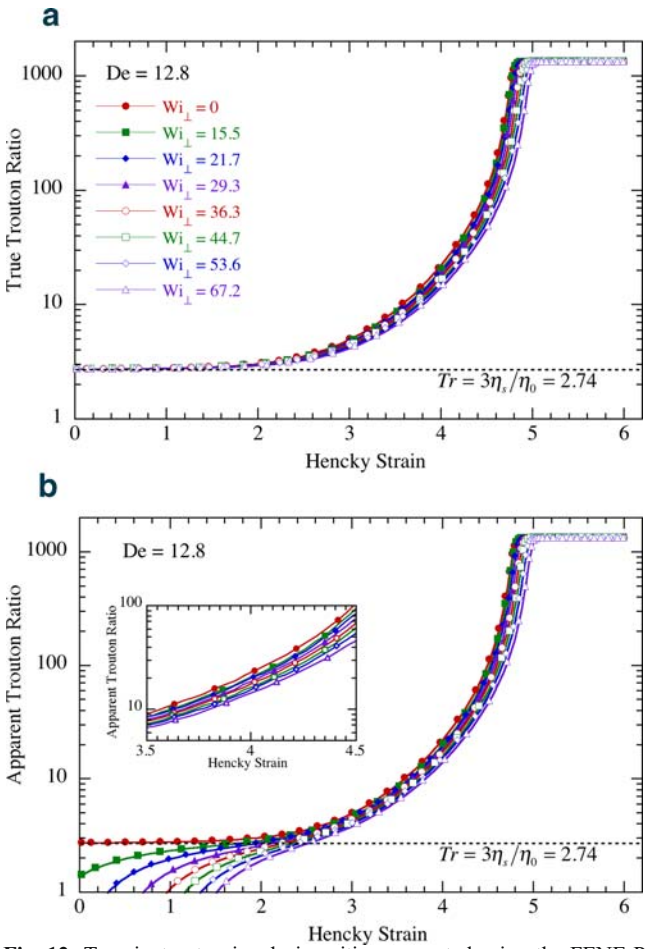


**Fig. 12** Transient extensional viscosities computed using the FENE-P model after applying a steady torsional flow. The fluid parameters correspond to the PS025 fluid, and the Deborah number for the stretching portion is fixed at De=12.8. **a** True Trouton ratio computed using principal tensile stress difference (Eq. 22) and **b** the apparent Trouton ratio computed using full force balance (cf. Eq. 21); (*filled circle*, $Wi_{\perp}$=0; *filled square*, $Wi_{\perp}$=15.5; *filled diamond*, $Wi_{\perp}$=21.7; *filled triangle*, $Wi_{\perp}$=29.3; *open circle*, $Wi_{\perp}$=36.3; *open square*, $Wi_{\perp}$=44.7; *open diamond*, $Wi_{\perp}$=53.6; *open triangle*, $Wi_{\perp}$=67.2). The *inset* shows a magnified view of the effect of pre-stretching on the transient stress growth

are unaffected by the initial pre-shearing flow, but the rate of growth of the transient extensional stresses is reduced as $Wi_{\perp}$ increases. At the highest Weissenberg number, the magnitude of the extensional viscosity can be as low as 44% of the corresponding value for $Wi_{\perp}=0$ at intermediate strain values ($3<\varepsilon<5$).

In a real filament stretching experiment, the only observable quantity is the total tensile force exerted on the endplate. Examination of the complete force balance on the stretching fluid filament, given in Eq. 21, reveals that this total force measurement contains both the principal and the secondary tensile stress differences. Without any additional measurements, it is impossible to decouple these two stress differences and extract the "true" Trouton ratio. The "apparent" Trouton ratio computed from the total tensile force is thus given by

$$\mathrm{Tr}_{\mathrm{app}} = \frac{\langle \tau_{zz} - \tau_{rr} \rangle + \frac{1}{2}\langle \tau_{rr} - \tau_{\theta\theta} \rangle}{\eta_0 \dot{\varepsilon}_0} \tag{31}$$

This apparent Trouton ratio is computed from the results of the FENE-P simulations, and the results are shown in Fig. 12b. The effect of pre-shearing on $\mathrm{Tr}_{\mathrm{app}}$ is much more pronounced at lower Hencky strains than it is on $\mathrm{Tr}_{\mathrm{true}}$. In this case, the steady-state Trouton ratio obtained at large Hencky strains ($\varepsilon \geq 6$) is still unaffected by the pre-shear conditions, but the initial plateau at small strains decreases with increasing $Wi_{\perp}$ and can even be negative initially. The delay in the onset of strain hardening is approximately the same as that observed in Fig. 12a for the "true" Trouton ratio. In both cases, the Hencky strain needed to achieve a Trouton ratio of Tr≈100 differs by up to $\Delta\varepsilon \approx 0.21$ strain units between the limit $Wi_{\perp} = 0$, in which no pre-rotation is imposed, and the maximum value of $Wi_{\perp}$. The magnitude of the pre-shearing effect that is predicted by the FENE-P constitutive model qualitatively captures trends observed experimentally. The magnitude of the delay of strain hardening is somewhat less than that observed in experiments, although the FENE-P and similar single mode models are known to strain-harden much more slowly at moderate strains than experiments show, even without pre-shear (Anna et al. 2001; Ghosh et al. 2001). In our experiments, strain hardening can be delayed by up to $\Delta\varepsilon \approx 0.59$ strain units, as compared with $\Delta\varepsilon \approx 0.21$ strain units predicted by the FENE-P simulations. The delay can be attributed to the large negative value of the secondary tensile stress difference, $\langle \tau_{rr} - \tau_{\theta\theta} \rangle$, that is present initially upon cessation of shearing. The principal tensile stress difference, $\langle \tau_{zz} - \tau_{rr} \rangle$, begins to grow immediately upon inception of stretching, but its growth is delayed as $\langle \tau_{rr} - \tau_{\theta\theta} \rangle$ relaxes back toward zero. In experiments, the large reduction in the initial measured Trouton ratio is not observed, most likely due (1) to the overshoot in the tensile force caused by lubrication effects (Spiegelberg et al. 1996), (2) the more rapid relaxation in the stress associated with higher relaxation modes, and (3) the neglect in our calculations of radial variations in the stress distribution.

## Conclusions

In this paper, we have investigated the consequences of systematically introducing a controlled pre-deformation history to a nearly ideal uniaxial extensional flow, as realized in a filament stretching rheometer. Two different types of pre-deformation history have been examined: first, oscillatory squeezing flow with the principal flow direction

along the axis of the filament stretching flow, and second, a steady torsional flow with the principal flow direction orthogonal to the direction of filament stretching. We have demonstrated that the two modes of initial deformation yield a fluid response consistent with the material functions measured using conventional shear rheometry. We have examined the effect of these two pre-shear modes by experimentally varying the deformation rate before stretching while keeping the subsequent elongation rate fixed. We observe that pre-straining due to an oscillatory axial squeezing flow leads to accelerated strain hardening in the transient tensile stress growth especially at moderate oscillation frequencies. On the other hand, pre-shearing orthogonal to the stretching direction leads to significant delays in strain hardening. While orthogonal pre-shearing leads to a greater maximum delay in the onset of strain hardening ($\Delta\varepsilon \approx 0.5$) than the maximum enhancement caused by oscillatory pre-straining ($\Delta\varepsilon \approx 0.2$), neither pre-shearing effect is found to be as large as that predicted by Brownian dynamics simulations due to differences in solvent quality ($\Delta\varepsilon \approx 1.0$; Li and Larson 2000). In the case of oscillatory pre-stretching, this reflects the small amplitude of the oscillation, and thus, the absence of nonlinear effects. In the case of orthogonal pre-shearing, this reflects in part the limited available range of pre-shear rates, as spiral elastic flow instabilities were observed in our device at the highest shear rates.

We have performed calculations of the predicted effects of these two pre-deformation histories on a fluid element using the FENE-P constitutive model, and we find that even these simple calculations yield good qualitative agreement with the observed experimental trends. In fact, the magnitude of the enhancement (in oscillatory squeeze flow) and retardation (in steady torsional flow) of strain hardening are comparable to the magnitudes observed experimentally. Furthermore, the non-monotonic trend observed with increasing oscillation frequency is also predicted, with the maximum advancement in strain hardening observed at $\gamma_0 De_{\|} \approx 0.5$ for both experiments and predictions.

The effects of parallel oscillatory pre-straining and orthogonal rotational pre-shearing on the transient stress growth during filament stretching can be understood by considering the effect of each flow on the initial orientation of the polymer molecules. In oscillatory squeeze flow, the polymer chains accumulate a net initial orientation in the direction of stretching, leading to an accelerated approach to steady state during stretching. This effect is maximized at moderate frequencies when the fluid response is viscoelastic, and thus, the polymer stretch is out of phase with the oscillating strain. In steady torsional shear flow, the polymer molecules are significantly oriented orthogonal to the stretching direction, thus, requiring a larger strain to align and subsequently unravel the polymer chains once stretching begins. This pre-conditioning argument and the experimental observations shown in Figs. 7 and 9 are consistent with recent observations from Brownian dynamics simulations (Larson et al. 1999; Larson 2000; Ghosh et al. 2001, 2002). The magnitudes of the changes in the tensile stress in an elongating fluid element may be as large as 30–50%. Accurately capturing the effect of an upstream shearing deformation is of critical importance in spatially inhomogeneous but steady Eulerian flows (for example, the steady shear flow in the delivery tubing and nozzle upstream of a spinneret/spinline; Bechtel et al. 2001). The good qualitative agreement between experiments and calculations using a single-mode dumbbell model suggests that these effects can be captured by existing nonlinear constitutive equations.

**Acknowledgments** This research was supported by NASA under Grants Nos. NAG3-1385 and NCC3-610. S.L.A. thanks the Fannie and John Hertz Foundation for supporting her graduate studies.

## References

Agarwal US (2000) Effect of initial conformation, flow strength, and hydrodynamic interaction on polymer molecules in extensional flows. J Chem Phys 113:3397–3403

Anna SL, Rogers C, McKinley GH (1999) On controlling the kinematics of a filament stretching rheometer using a real-time active control mechanism. J Non-Newtonian Fluid Mech 87:307–335

Anna SL, McKinley GH, Nguyen DA, Sridhar T, Muller SJ, Huang J, James DF (2001) An interlaboratory comparison of measurements from filament-stretching rheometers using common test fluids. J Rheol 45:83–114

Avagliano A, Phan-Thien N (1996) Torsional flow: elastic instability in a finite domain. J Fluid Mech 312:279–298

Avagliano A, Phan-Thien N (1999) Torsional flow stability of highly dilute polymer solutions. J Non-Newtonian Fluid Mech 84:19–44

Babcock HP, Teixeira RE, Hur JS, Shaqfeh ESG, Chu S (2003) Visualization of molecular fluctuations near the critical point of the coil–stretch transition in polymer elongation. Macromolecules 36:4544–4548

Bach A, Almdal K, Rasmussen HK, Hassager O (2003a) Elongational viscosity of narrow molar mass distribution polystyrene. Macromolecules 36:5174–5179

Bach A, Rasmussen HK, Hassager O (2003b) Extensional viscosity for polymer melts measured in the filament stretching rheometer. J Rheol 47:429–441

Bechtel SE, Youssef NT, Forest MG, Zhou H, Koelling KW (2001) Non-Newtonian viscous oscillating free surface jets, and a new strain-rate dependent viscosity form for flows experiencing low strain rates. Rheol Acta 40:373–383

Beck VA, Shaqfeh ESG (2006) Ergodicity breaking and conformational hysteresis in the dynamics of a polymer tethered at a surface stagnation point. J Chem Phys 124:16

Bhardwaj A, Richter D, Rothstein JP (2007) The effect of pre-shear on the extensional rheology of wormlike micelle solutions. Rheol Acta 46:861–875

Bhattercharjee PK, Oberhauser JP, McKinley GH, Leal LG, Sridhar T (2002) Extensional rheometry of entangled solutions. Macromolecules 35:10131–10148

Bhattacharjee PK, Nguyen DA, McKinley GH, Sridhar T (2003) Extensional stress growth and stress relaxation in entangled polymer solutions. J Rheol 47:269–290

Binding DM (1993) Contraction flows and new theories for estimating extensional viscosity. In: Collyer AA (ed) Techniques in rheological measurement. Chapman & Hall, London, pp 1–32

Bird RB, Armstrong RC, Hassager O (1987a) Dynamics of polymeric liquids, vol 1: fluid mechanics. Wiley, New York

Bird RB, Curtiss CF, Armstrong RC, Hassager O (1987b) Dynamics of polymeric liquids, vol 2: kinetic theory. Wiley Interscience, New York

Boger DV (1977/1978) A highly elastic constant-viscosity fluid. J Non-Newtonian Fluid Mech 3:87–91

Brandrup J, Immergut EH, Grulke EA (eds) (1999) In: Polymer handbook. Wiley, New York

Byars JA, Öztekin A, Brown RA, McKinley GH (1994) Spiral instabilities in the flow of highly elastic fluids between rotating parallel disks. J Fluid Mech 271:173–218

Calado VMA, White JM, Muller SJ (2005) Transient behavior of Boger fluids under extended shear flow in a cone-and-plate rheometer. Rheol Acta 44:250–261

Dimitropoulos CD, Dubief Y, Shaqfeh ESG, Moin P, Lele SK (2005) Direct numerical simulation of polymer-induced drag reduction in turbulent boundary layer flow. Phys Fluids 17:011705.1–011705.4

Donohue GL, Tiederman WG, Reischman MM (1972) Flow visualization of the near-wall region in a drag-reducing channel flow. J Fluid Mech 56:559–575

Doyle PS, Shaqfeh ESG, McKinley GH, Spiegelberg SH (1998) Relaxation of dilute polymer solutions following extensional flow. J Non-Newtonian Fluid Mech 76:79–110

Dubief Y, White CM, Terrapon VE, Shaqfeh ESG, Moin P, Lele SK (2004) On the coherent drag-reducing and turbulence-enhancing behaviour of polymers in wall flows. J Fluid Mech 514:271–280

Eggers J (1993) Universal pinching of 3d axisymmetrical free-surface flow. Phys Rev Lett 71:3458–3460

Eggers J, Dupont TF (1994) Drop formation in a one-dimensional approximation of the Navier–Stokes equation. J Fluid Mech 262:205–221

Evans AR, Shaqfeh ESG, Frattini PL (1994) Observations of polymer conformation during flow through a fixed fibre bed. J. Fluid Mech 281:319–356

Ferguson J, Hudson NE, Forsyth JF (1998) Transient extensional rheology and the influence of strain history. J Non-Newtonian Fluid Mech 79:213–223

Field JS, Swain MV, Phan-Thien N (1996) An experimental investigation of the use of random squeezing to determine the complex modulus of viscoelastic fluids. J Non-Newtonian Fluid Mech 65:177–194

Flory PJ (1953) Principles of polymer chemistry. Cornell University Press, Ithaca

Fuller GG, Leal LG (1980) Flow birefringence of dilute polymer-solutions in two-dimensional flows. Rheol Acta 19:580–600

Ghosh I, McKinley GH, Brown RA, Armstrong RC (2001) Deficiencies of FENE dumbbell models in describing the rapid stretching of dilute polymer solutions. J Rheol 45:721–758

Ghosh I, Joo YL, McKinley GH, Brown RA, Armstrong RC (2002) A new model for dilute polymer solutions in flows with strong extensional components. J Rheol 46:1057–1089

Graham MD (2004) Drag reduction in turbulent flow of polymer solutions. In: Binding DM, Walters K (eds) Rheology reviews. British Society of Rheology, UK, pp 143–170

Gupta RK, Nguyen DA, Sridhar T (2000) Extensional viscosity of dilute polystyrene solutions: Effect of concentration and molecular weight. Phys Fluids 12:1296–1318

Hermansky CG, Boger DV (1995) Opposing-jet viscometry of fluids with viscosity approaching that of water. J Non-Newtonian Fluid Mech 56:1–14

Hoffman BD, Shaqfeh ESG (2007) The dynamics of the coil–stretch transition for long, flexible polymers in planar mixed flows. J Rheol 51:947–969

Housiadas KD, Beris AN, Handler RA (2005) Viscoelastic effects on higher order statistics and on coherent structures in turbulent channel flow. Phys Fluids 17:035106.1–035106.20

Hsieh CC, Larson RG (2004) Modeling hydrodynamic interaction in Brownian dynamics: simulations of extensional and shear flows of dilute solutions of high molecular weight polystyrene. J Rheol 48:995–1021

Hsieh CC, Larson RG (2005) Prediction of coil–stretch hysteresis for dilute polystyrene molecules in extensional flow. J Rheol 49:1081–1089

Hsieh CC, Li L, Larson RG (2003) Modeling hydrodynamic interaction in Brownian dynamics: simulations of extensional flows of dilute solutions of DNA and polystyrene. J Non-Newtonian Fluid Mech 113:147–191

Hur JS, Shaqfeh ESG, Babcock HP, Chu S (2002) Dynamics and configurational fluctuations of single DNA molecules in linear mixed flows. Phys Rev E 66:011915

Ilg P, De Angelis E, Karlin IV, Casciola CM, Succi S (2002) Polymer dynamics in wall turbulent flow. Europhys Lett 58:616–622

James DF, Walters K (1994) A critical appraisal of available methods for the measurement of extensional properties of mobile systems. In: Collyer AA (ed) Techniques of rheological measurement. Elsevier, New York, pp 33–53

James DF, McLean BD, Saringer JH (1987) Presheared extensional flow of dilute polymer solutions. J Rheol 31:453–481

Jones DM, Walters K (1989) The behaviour of polymer solutions in extension-dominated flows, with applications to enhanced oil recovery. Rheol Acta 28:482–498

Jones DM, Walters K, Williams PR (1987) On the extensional viscosity of mobile polymer solutions. Rheol Acta 26:20–30

Larson RG (2000) The role of molecular folds and 'pre-conditioning' in the unraveling of polymer molecules during extensional flow. J Non-Newtonian Fluid Mech 94:37–45

Larson RG (2005) The rheology of dilute solutions of flexible polymers: progress and problems. J Rheol 49:1–70

Larson RG, Magda JJ (1989) Coil–stretch transitions in mixed shear and extensional flows of dilute polymer solutions. Macromolecules 22:3004–3010

Larson RG, Hu H, Smith DE, Chu S (1999) Brownian dynamics simulations of a DNA molecule in an extensional flow field. J Rheol 43:267–304

Lee EC, Muller SJ (1999) Flow light scattering studies of polymer coil conformation in solutions in extensional flow. Macromolecules 32:3295–3305

Li L, Larson R (2000) Excluded volume effects on the birefringence and stress of dilute polymer solutions in extensional flow. Rheol Acta 39:419–427

Magda JJ, Larson RG, Mackay ME (1988) Deformation-dependent hydrodynamic interaction in flows of dilute polymer solutions. J Chem Phys 89:2504–2513

Magda JJ, Lou J, Baek SG, Devries KL (1991) Second normal stress difference of a Boger fluid. Polymer 32:2000–2009

Massah H, Kontomaris K, Schowalter WR, Hanratty TJ (1993) The configurations of a FENE bead-spring chain in transient rheological flows and in a turbulent flow. Phys Fluids A 5:881–890

McKinley GH, Sridhar T (2002) Filament-stretching rheometry of complex fluids. Annu Rev Fluid Mech 34:375–415

Nielsen JK, Rasmussen HK, Hassager O, McKinley GH (2006) Elongational viscosity of monodisperse and bidisperse polystyrene melts. J Rheol 50:453–476

Orr NV, Sridhar T (1999) Probing the dynamics of polymer solutions in extensional flow using step strain rate experiments. J Non-Newtonian Fluid Mech 82:203–232

Petrie CJS (1995) Extensional flow—a mathematical perspective. Rheol Acta 34:12–26

Petrie CJS (2006) One hundred years of extensional flow. J Non-Newtonian Fluid Mech 137:1–14

Phan-Thien N (1980) Small strain oscillatory squeeze film flow of simple fluids. J Austral Math Soc Series B 22:22–27

Phan-Thien N, Dudek J, Boger DV, Tirtaatmadja V (1985) Squeeze film flow of ideal elastic liquids. J Non-Newtonian Fluid Mech 18:227–254

Prabhakar R, Prakash JR (2006) Gaussian approximation for finitely extensible bead-spring chains with hydrodynamic interaction. J Rheol 50:561–593

Prabhakar R, Prakash JR, Sridhar T (2006) Effect of configuration-dependent intramolecular hydrodynamic interaction on elastocapillary thinning and breakup of filaments of dilute polymer solutions. J Rheol 50:925–947

Press WH, Teukolsky SA, Vetterling WT, Flannery BP (1992) Numerical recipes in C: the art of scientific computing. Cambridge University Press, Cambridge

Ramanan VV, Bechtel SE, Gauri V, Koelling KW, Forest MG (1997) Exploiting accurate spinline measurements for elongational material characterization. J Rheol 41:283–306

Rasmussen HK, Nielsen JK, Bach A, Hassager O (2005) Viscosity overshoot in the start-up of uniaxial elongation of low density polyethylene melts. J Rheol 49:369–381

Renardy M (1994) Some comments on the surface-tension driven breakup (or the lack of it) of viscoelastic jets. J Non-Newtonian Fluid Mech 51:97–107

Rothstein JP (2003) Transient extensional rheology of wormlike micelle solutions. J Rheol 47:1227–1247

Rothstein JP, McKinley GH (2000) Non-isothermal effects on the flow stability of the torsional flow of highly elastic fluids. Phys Fluids 13:382–396

Rothstein JP, McKinley GH (2002a) A comparison of the stress and birefringence growth of dilute, semi-dilute and concentrated polymer solutions in uniaxial extensional flows. J Non-Newtonian Fluid Mech 108:275–290

Rothstein JP, McKinley GH (2002b) Inhomogeneous transient uniaxial extensional rheometry. J Rheol 46:1419–1443

Satrape JV, Crochet MJ (1994) Numerical simulation of the motion of a sphere in a Boger fluid. J Non-Newtonian Fluid Mech 55:91–111

Schroeder CM, Babcock HP, Shaqfeh ESG, Chu S (2003) Observation of polymer conformation hysteresis in extensional flow. Science 301:1515–1519

Schroeder CM, Shaqfeh ESG, Chu S (2004) Effect of hydrodynamic interactions on DNA dynamics in extensional flow: simulation and single molecule experiment. Macromolecules 37:9242–9256

Schroeder CM, Teixeira RE, Shaqfeh ESG, Chu S (2005) Dynamics of DNA in the flow-gradient plane of steady shear flow: observations and simulations. Macromolecules 38:1967–1978

Smith DE, Chu S (1998) Response of flexible polymers to a sudden elongational flow. Science 281:1335–1340

Solomon MJ, Muller SJ (1996a) Flow past a sphere in polystyrene-based Boger fluids: the effect on the drag coefficient of finite extensibility, solvent quality and polymer molecular weight. J Non-Newtonian Fluid Mech 62:81–94

Solomon MJ, Muller SJ (1996b) Study of mixed solvent quality in a polystyrene–dioctyl phthalate–polystyrene system. J Poly Sci B Polym Phys 34:181–192

Spiegelberg SH, Ables DC, McKinley GH (1996) The role of end-effects on measurements of extensional viscosity in viscoelastic polymer solutions with a filament stretching rheometer. J Non-Newtonian Fluid Mech 64:229–267

Sridhar T (1990) An overview of the project M1. J Non-Newtonian Fluid Mech 35:85–92

Sridhar T, Nguyen DA, Fuller GG (2000) Birefringence and stress growth in uniaxial extension of polymer solutions. J Non-Newtonian Fluid Mech 90:299–315

Sridhar T, Nguyen DA, Prabhakar R, Prakash JR (2007) Rheological observation of glassy dynamics of dilute polymer solutions near the coil–stretch transition in elongational flows. Phys Rev Lett 98:167801

Sridhar T, Tirtaatmadja V, Nguyen DA, Gupta RK (1991) Measurement of extensional viscosity of polymer solutions. J Non-Newtonian Fluid Mech 40:271–280

Stone PA, Roy A, Larson RG, Waleffe F, Graham MD (2004) Polymer drag reduction in exact coherent structures of plane shear flow. Phys Fluids 16:3470–3482

Sunthar P, Nguyen DA, Dubbelboer R, Prakash JR, Sridhar T (2005) Measurement and prediction of the elongational stress growth in a dilute solution of DNA molecules. Macromolecules 38:10200–10209

Szabo P (1997) Transient filament stretching rheometer I: force balance analysis. Rheol Acta 36:277–284

Szabo P, McKinley GH (2003) Filament stretching rheometer: inertia compensation revisited. Rheol Acta 42:269–272

Tiederman WG, Luchik TS, Bogard DG (1985) Wall-layer structure and drag reduction. J Fluid Mech 156:419–437

Tirtaatmadja V, Sridhar T (1993) A filament stretching device for measurement of extensional viscosity. J Rheol 37:1081–1102

Toms BA (1977) Early experiments on drag reduction by polymers. Phys Fluids 20:S3–S5

Tripathi A, Tam KC, McKinley GH (2006) Rheology and dynamics of associative polymers in shear and extension: theory and experiments. Macromolecules 39:1981–1999

Vissmann K, Bewersdorff H-W (1990) The influence of pre-shearing on the elongational behaviour of dilute polymer and surfactant solutions. J Non-Newtonian Fluid Mech 34:289–317

Vorwerk J, Brunn PO (1991) Porous medium flow of the fluid A1: effects of shear and elongation. J Non-Newtonian Fluid Mech 41:119–131

Woo NJ, Shaqfeh ESG (2003) The configurational phase transitions of flexible polymers in planar mixed flows near simple shear. J Chem Phys 119:2908–2914

Ye X, Sridhar T (2001) Shear and extensional properties of three-arm polystyrene solutions. Macromolecules 34:8270–8277

Ye X, Larson RG, Pattamaprom C, Sridhar T (2003) Extensional properties of monodisperse and bidisperse polystyrene solutions. J Rheol 47:443–468

Zhou Q, Akhavan R (2003) A comparison of FENE and FENE-P dumbbell and chain models in turbulent flow. J Non-Newtonian Fluid Mech 109:115–155